

Øyvind Antonsen

Unsteady flow in wicket gate and runner with focus on static and dynamic load on runner

Thesis for the degree of philosophiae doctor

Trondheim, September 2007

Norwegian University of
Science and Technology
Faculty of Engineering Science and Technology
The Department of Energy and Process Engineering

NTNU
Norwegian University of Science and Technology

Thesis for the degree of philosophiae doctor

Faculty of Engineering Science and Technology
The Department of Energy and Process Engineering

©Øyvind Antonsen

ISBN 978-82-471-3392-7 (printed ver.)
ISBN 978-82-471-3408-5 (electronic ver.)
ISSN 1503-8181

Theses at NTNU, 2007:155

Printed by Tapir Uttrykk

Abstract

This thesis presents a study on unsteady flow at the inlet of the runner in a Francis turbine. The main goal has been to find a connection between the design of the wicket gate and the dynamic load on the runner due to rotor stator interaction. The working hypothesis has been based on the theory that correct profiling of the wicket gate can make the pressure distribution at the inlet of the runner more uniform, and hence, reduce the dynamic load on the runner.

Velocity measurements by means of Laser Doppler Anemometry (LDA) have been carried out in a cascade rig with different wicket gate profiling. Also, the pressure around the surface of one wicket gate has been measured. CFD calculations, validated with the LDA-measurements, have been used to calculate the pressure distribution at the inlet of the runner with different profiling of the wicket gate and the corresponding load on the runner.

The LDA measurements have shown that the wake in a turbine cascade follows the classic wake theory fairly well. The wakes tends to mix out faster than according to the wake theory, due to the accelerated flow field. The CFD results deviate somewhat from the LDA measurements, but have shown good agreement with relative changes in the geometry. The 2D CFD calculations under-estimates the depth of the wake with ca 25 % while with 3D calculations the deviation is about 10 %, which has been considered to be good agreement.

Due to this consideration, it has been found trustworthy to use CFD to compare pressure distribution with different profiling of the wicket gate. The results show that by profiling the guide vanes asymmetric with the 'flat' side pointing toward the runner, the pressure distribution becomes more uniform. This is also shown by the pressure measurements around the guide vane profile.

A simplified CFD-calculation of guide vane/runner interaction has shown that a more uniform pressure distribution at the inlet of the runner will reduce the dynamic load variation on the runner blade without increasing the losses in the flow.

Acknowledgments

The work presented in this thesis has been performed at the Hydro Power Laboratory, Department of Energy and Process Engineering at the Norwegian University of Science and Technology (NTNU).

During the work with this thesis, a number of people have contributed with advice, support and encouragement. I would hereby like to thank you all for your help. Especially my supervisor, Professor Torbjørn Nielsen, for making this study possible, for valuable discussions and for guiding me in the right directions in the times when I was lost. Associate Professor Ole Gunnar Dahlhaug for valuable discussions. Bård Brandastrø, Joar Grillstad, Ellef Bakken and Trygve Oppheim for help with installations, instrumenting and operating of the test rig. Wenche Johansen for keeping track of all my deadlines and other administrative challenges. My fellow PhD-students Sølvi Eide and Kristin Pettersen for valuable discussions. Thanks also to Morten Kjeldsen at FDB for including me in experiments at an early stage of the study and for valuable discussions and support through the whole study. Thanks to Per Egil Skåre at Sintef for help with Matlab and Fluent. Thanks to Rune Engeskau at Sintef for lending me a ColorLink in an urgent moment.

Thanks to the Research Council of Norway and to GE Energy for funding the project. Thanks also to GE for giving me access to their models and geometry, lending me measuring instruments and to their employers who have spent much time helping me. Jan Tore Billdal, Sebastian Videhult, Terje Løvseth, Kjell Sivertsen and Einar Sundsvold in particular.

Thanks to my good friend Tom Farnen for valuable help with the proofreading.

Finally, I want to express my deep gratitude to my wife Eli for being patience with me, supporting, and encouraging me whenever needed. Thank you!

Contents

Abstract	i
Acknowledgments	iii
Contents	v
List of figures	vii
List of tables	ix
Nomenclature	xi
1 Introduction	1
1.1 Background	1
1.2 Hypothesis	2
1.3 Outline	3
2 Theoretical background	5
2.1 Francis turbine	5
2.2 Sources of instability	9
2.3 Previous work	12
2.4 Wake flow	15
3 Numerical model	21
3.1 Model details	21
3.2 Results	25
3.2.1 Mesh dependency	25
3.2.2 Turbulence model dependency	28

3.2.3	Pressure distribution	28
4	Experiment	33
4.1	Experimental set-up	34
4.1.1	LDA principles and rig setup	34
4.1.2	Flow measurement	39
4.1.3	Guide vane pressure-profile	39
4.2	Experimental results	42
4.2.1	Guide vane pressure-profile	44
4.2.2	Wake plots	46
4.2.3	Normalized results	51
4.2.4	Wake in span-wise direction	55
4.3	Summary	58
4.4	Estimated experimental uncertainty	58
5	Comparison of numerical and experimental results	61
5.1	Comparison	61
5.2	Additional CFD-calculations	69
5.3	Summary	74
6	Conclusions and further work	75
6.1	Conclusions	75
6.2	Further work	76
	Bibliography	79
	Appendices	87
A	Papers	I
A.1	IAHR Stockholm, Sweden, 2004	II
A.2	Hydrovision Portland, Oregon, USA, 2006	XII
A.3	IAHR Yokohama Japan, 2006	XXIII

List of Figures

2.1	Layout and energy trade in a hydro power plant	6
2.2	Axial and radial sketch of a high head Francis turbine	6
2.3	Runner blade shape vs. reaction ratio	8
2.4	Energy trade	8
2.5	Pressure side and suction side	9
2.6	Velocity diagram at inlet Francis runner	10
2.7	Lift and drag force on a wing profile	16
2.8	Wake behind a body	16
2.9	Regions in wake flow	17
2.10	Wave and runner propagation	19
3.1	Calculation area	22
3.2	Mesh around one guide vane	23
3.3	The different layers in the near wall region	25
3.4	Pressure distribution vs. mesh size	26
3.5	Wake vs. mesh size	27
3.6	Results from different turbulence models	29
3.7	Pressure distribution outlet GVs with different guide vane profiles	30
3.8	Pressure distribution inlet runner with different guide vane profiles	30
3.9	GV profiles	31
4.1	The cascade rig	34
4.2	LDA principles	36
4.3	LDA set-up	37
4.4	LDA measurements	37
4.5	Guide vane profiles	38
4.6	Vertical view of the guide vane profile	39

4.7	Pitot taps at the inlet pipe	40
4.8	Instrumented guide vane	41
4.9	Velocity from pitot measurements	42
4.10	Spanwise velocity profile	45
4.11	Pressure coefficients	47
4.12	Wake plots	48
4.13	Best fit coefficient	53
4.14	Normalized velocity defect vs. downstream distance	53
4.15	Measured data vs. wake theory	54
4.16	Wake in span wise direction	56
4.17	Wake in span wise direction	57
5.1	Wake from LDA and CFD	62
5.2	Complete geometry	64
5.3	Simplified geometry	64
5.4	Pressure plot from different simplifications	65
5.5	3D Mesh around the guide vane	66
5.6	Wakes from 3D CFD	67
5.7	Span wise wake from 3D CFD	67
5.8	Normalized CFD results	68
5.9	Simplified geometry	69
5.10	Velocity vectors at the inlet of the runner blade	70
5.11	Torque vs. time	71
5.12	Torque on runner blade	72

List of Tables

- 4.1 LDA Characteristics (in water) 36
- 4.2 Abbreviations 44
- 4.3 Test matrix for guide vane measurements 44

- 5.1 Results for different guide vane profiling 73

Nomenclature

Symbol	Quantity	Unit
A	Area	m^2
a	Speed of sound	m/s
a, b, c, d	Coefficients	-
B	Geometric shape factor	-
b	Width of wake	m
C_D	Drag coefficient	-
C_f	Skin friction coefficient	-
C_L	Lift coefficient	-
C_p	Pressure coefficient	-
c	Chord length	m
c	Velocity	m/s
c_m	Meridional Velocity	m/s
c_t	Tangential velocity	m/s
c_u	Circumferential velocity	m/s
D	Outlet diameter of the turbine runner	m
d	Diameter	m
d_f	Fringe spacing	μm
F	Force	N
F	Total error	-
f	Frequency	Hz
f_n	Frequency of turbine runner	Hz
g	Gravity constant	m/s^2
H	Head	m
H_n	Net head	m

Symbol	Quantity	Unit
h	Pressure head	m
h	Height	m
L	Length	m
n	Rotational speed of turbine runner	rpm
P	Power	W
P	Mean pressure	Pa
p	Pressure	Pa
Q	Flow rate	m ³ /s
R	Radius	m
r	Radius	m
Re	Reynolds number	-
s	Distance	m
St	Strouhal number	-
t	Thickness	m
t	Time	s
U	Velocity	m/s
U, V, W	Mean velocities in x,y and z directions respectively	m/s
u, v, w	Velocities in x,y and z directions respectively	m/s
u_τ	Friction velocity	m/s
V	True value	-
W	Relative velocity	m/s
X	Sample average	-
x, y, z	Cartesian coordinates	m
y^+	Dimensionless distance from wall	-
Z_r	Number of runner blades	-
Z_{GV}	Number of guide vanes	-

Greek letters

α	Guide vane opening angle	°
β	Inlet flow angle	°
δ	Boundary layer thickness	m
η	Hydraulic efficiency	-
λ	Wave length	m
ω	Angular velocity of turbine runner	rad/s
Ω	Speed number	-

Symbol	Quantity	Unit
ϕ	Angle variation	°
ρ	Density	kg/m ³
μ	Dynamic viscosity	kg/ms
ν	Kinematic viscosity	m ² /s
τ	Shear stress	Pa
τ_w	Shear stress at wall	Pa
θ	Laser angle of incidence	°

Subscripts

∞	Free stream properties
1	Inlet of the runner
2	Outlet of the runner
3	Outlet of the draft tube
GV	Guide vane
h	Hydraulic
i	Inlet
o	Outlet
norm	Normalized value
r	Runner
v	Virtual values
w	Values at a wall

Superscripts

*	Values at best efficiency point
n	Exponential constant

Abbreviations

2D	2-dimensional
3D	3-dimensional

Symbol	Quantity	Unit
BEP	Best efficiency point of a turbine	
CFD	Computational fluid dynamics	
FFT	Fast fourier transform	
GV	Guide vane	
LE	Leading edge	
LDA	Laser Doppler Anemometry	
mWc	Meter water column	
NTNU	Norwegian University of Science and Technology	
ref	Reference	
rms/r.m.s	Root mean square	
TE	Trailing edge	
Tu	Turbulence intensity	
PIV	Particle image velocimetry	
RSI	Rotor stator interaction	

Overlined values are mean values, e.g \bar{u} as mean velocity

Chapter 1

Introduction

1.1 Background

For turbines in water power plants, the trends toward higher speed and higher power output per kg unit have increased the potential for fluid/structure interaction problems, and the severity of those problems. Under certain conditions these interaction phenomena can lead to structural failure on the runner blades. Turbine manufactures have in recent years experienced several serious runner blade cracking due to high dynamic stress level at the runner inlet. In Francis turbines, the main source of instability at the boundary between the guide vanes and the runner is the wake flow from the guide vanes that is chopped by the runner blades, causing oscillating forces. Due to their large number of cycles, these forces can cause severe damage even with small amplitudes. An improved prediction of these dynamic forces would be of great value in order to avoid fatigue problems on the runners in the future.

Also the trends in the power market, especially in Norway, have made it more desirable to run the turbine on a larger operational area, not only at the best efficiency point, for which most of the old turbines are designed for. More operation time at part load and full load will increase the probability of damage due to instability.

Refurbishment and upgrading of old power plants will often lead to increased

flow, more power output, changes in operational pattern, and it is important to have knowledge in what way these factors govern the pressure pulses. Generally the main focus is on the efficiency, but care should also be taken to avoid high pressure pulses in order to reduce maintenance costs. By increasing the knowledge of the pressure pulses and their governing factors, the turbines may run smoothly over the whole operation area.

1.2 Hypothesis

It is assumed that the main source of pressure pulses at the inlet of the runner is caused by the interaction between the rotating runner and the stationary wicket gates. From a rotating frame of reference, a runner blade will experience a change in the flow field each time it is passing one wicket gate. This will cause a varying load on the runner blade, dependent of the rotational speed of the runner and number of wicket gates.

From a static frame of reference, a pressure variation will occur each time a runner blade is passing a guide vane. A stationary point will experience a varying pressure depending of the rotational speed of the runner and number of runner blades.

The dynamic force acting on the runner blade due to the presence of the wicket gate is assumed to be dominated by two different effects; the viscous effect and the pressure effect. The viscous effect is due to the velocity defect in the flow due to the shadow from the upstream wicket gate.

The pressure effect can be visualized by thinking of the fact that the wicket gate having one side pointing toward the spiral casing where the energy in the water is mainly pressure energy. The other side of the wicket gate is pointing toward the runner where pressure is reduced due to the accelerated flow through the wicket gate. This will cause a pressure side and suction side on the wicket gate which will contribute to a non-uniform pressure distribution at the outlet of the wicket gate.

By profiling the wicket gate so a local pressure side and suction side are created in a way counteracting the global pressure, the overall pressure variation at the inlet of the runner might be reduced, resulting in less dynamic load at the inlet of the runner blade.

1.3 Outline

The main focus in this thesis has been the unsteady flow at the inlet of the runner in Francis turbines and forces on the runner due to this kind of flow. It has been emphasized to describe how the flow through the wicket gate will impact on the pressure pulses at the inlet of the runner and how the design of the wicket gate can worsen or improve these forces. It has also been emphasized to simplify the flow pattern as much as possible in order to investigate the phenomenon by means of fundamental fluid theory.

During the work on this thesis, three papers have been submitted and presented at various conferences. These papers represent the status of the work at the given time and also some work on the side of the main focus of the thesis. Due to the continuity of the thesis this material has been omitted from the main part of the thesis and will be presented in appendix A only.

Chapter 2

Theoretical background

A short introduction to the Francis turbine, fundamentals of wake flow, and a review of previous work will be given as a background and motivation for the work carried out in this thesis.

2.1 Francis turbine

Francis turbines are usually used in power plants with heads between ca 25 to 700 meter and is the most common turbine used in Norwegian power plants. A sketch of a typically high head power plant with a Francis turbine is shown in figure 2.1 on the following page, and a more detailed sketch of the different turbine parts are shown in figure 2.2.

The wicket gate consist of a number of vanes that can be adjusted in order to increase or reduce the flow rate through the turbine. The vanes are arranged between two parallel covers normal to the turbine shaft. The main purpose of the wicket gate is to adjust the load on the turbine by regulating the flow, secondary they give the water a spin around the rotating axis before is enters the runner.

There are some overlapping names on the wicket gate. The expression *Wicket gate* is often used on the whole set of guide vanes, while one or more guide vanes are simply called *guide vane* or *guide vanes*.

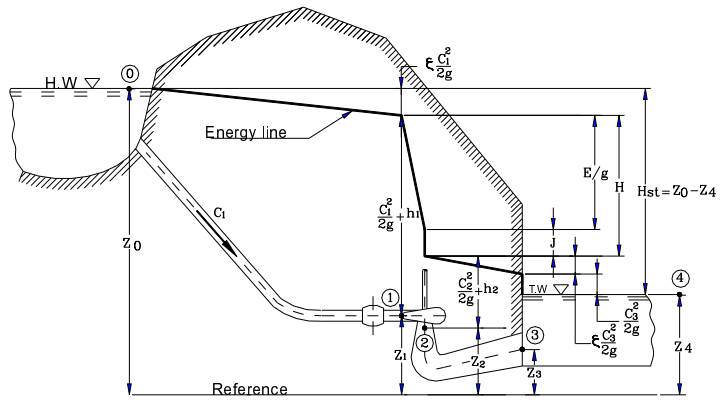


Figure 2.1: Layout and energy trade in a hydro power plant, from [11]

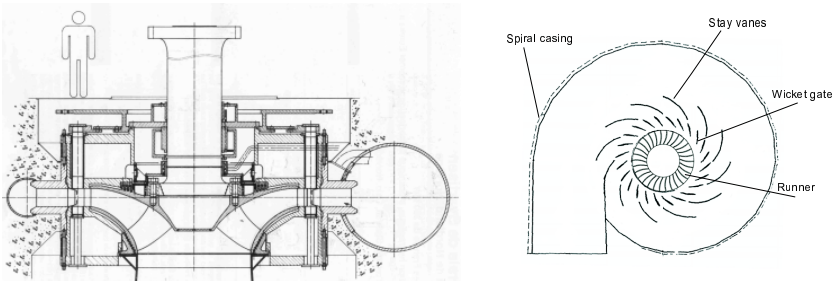


Figure 2.2: Axial and radial sketch of a high head Francis turbine

The available head in a power plant is given by the difference of the high water level and the tail water level and can be expressed as:

$$P = \rho g H Q \quad [\text{W}] \quad (2.1)$$

In more detail, losses in the process must be taken into consideration. The hydraulic efficiency of the turbine is defined as the ratio between the utilized head and the available head. By definition the available head is established by subtracting the total head at the outlet of the draft tube, from the total head at the inlet of the runner. By this definition, losses in the conduit system, head- and tail race tunnels are not included in the turbine efficiency. Figure 2.1 on the preceding page shows the power trade in a power plant, and from this figure the expression of the available head can be obtained:

$$H = \left(\frac{c_1^2}{2g} + h_1 + z_1 \right) - \left(\frac{c_3^2}{2g} + h_3 + z_3 \right) \quad [\text{m}] \quad (2.2)$$

The hydraulic efficiency of the turbine can then be expressed as:

$$\eta_h = \frac{H_n}{H} \quad [-] \quad (2.3)$$

Where H_n is the net head, accounted for losses developed in the turbine and draft tube.

At the inlet of the spiral casing, the energy is mainly pressure energy. The flow is evenly distributed around the circumference of the casing and passes the stay vanes and guide vanes before it enters the runner. Through the stay- and guide vanes the flow is accelerated, converting pressure energy to velocity energy. At the inlet of the runner the energy is typically 50% velocity energy and 50% pressure energy, depending on the reaction ratio of the turbine. The reaction ratio is defined as the pressure drop through the runner divided on the net head, see equation (2.4).

$$R = \frac{h_1 - h_2}{H} \quad [-] \quad (2.4)$$

In other words, the reaction ratio is the pressure part of the total energy converted into mechanical energy the runner, and for middle and high head Francis turbines the value is typically 0.48-0.50, dependent on the blade design, while for a Pelton turbine it is always zero since the pressure is the same before and after the runner. Figure 2.3 shows how the reaction ratio varies with the different shapes of the runner blade.

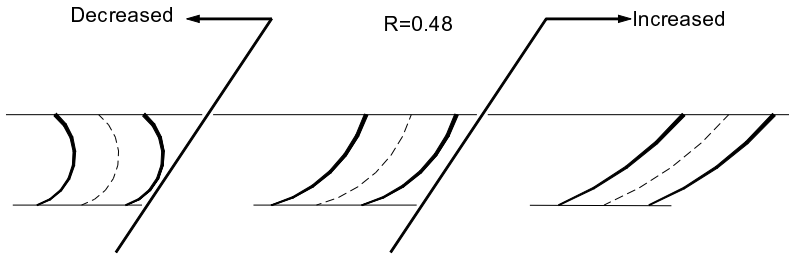


Figure 2.3: Runner blade shape vs. reaction ratio

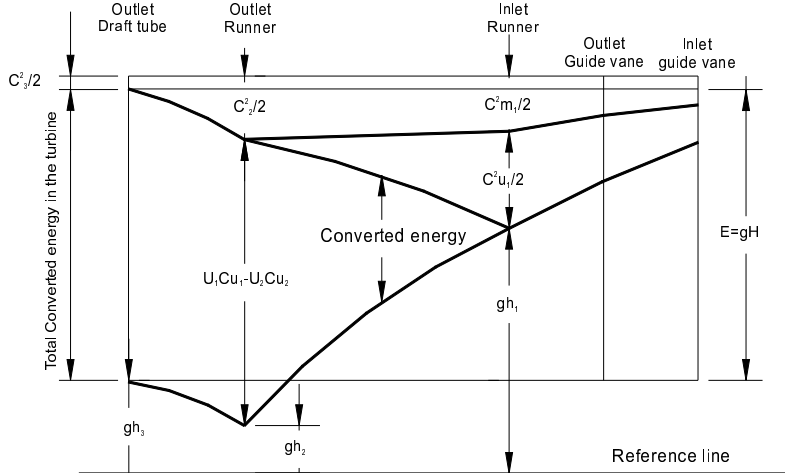


Figure 2.4: Energy trade

Figure 2.4 shows a detailed sketch of the energy conversion through a Francis turbine from the wicket gate outlet to the outlet of the draft tube. It can be seen from the figure that the meridional velocity increases toward a decreasing radius according to the law of continuity, and according to Bernoulli's equation the pressure energy must therefore decrease toward a decreasing radius. Due to this energy conversion, a guide vane will have a high pressure side and a low pressure side since two points located at the same chord length are located at different radii, see figure 2.5. The low pressure side is called suction side and the high pressure side is called pressure side. Due to this difference, the pressure and velocity distribution from guide vane to guide vane will be non-uniform as shown in the same figure.

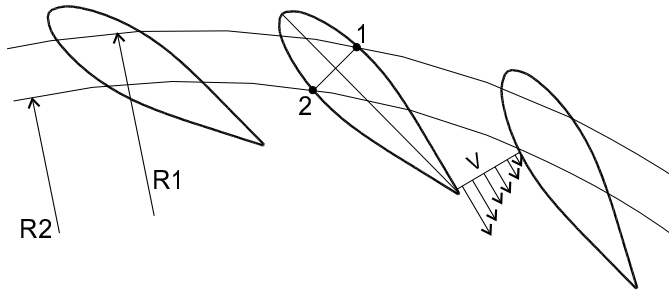


Figure 2.5: Pressure side and suction side, ref. figure 2.4.

In addition to regulating the flow, the guide vanes also gives the flow a spin around the rotational center before it enters the runner. Figure 2.6 on the following page shows a velocity diagram at the inlet of the runner. The angle α is the flow angel given by the position of the guide vanes and will vary as the wicket gate are opening or closing. At best efficiency point (BEP), the flow reaches the inlet of the runner blade with minimum impact losses.

2.2 Sources of instability

Instability at the inlet of the runner in a Francis turbine is a complex phenomenon with several factors impacting on the total load. The main focus in

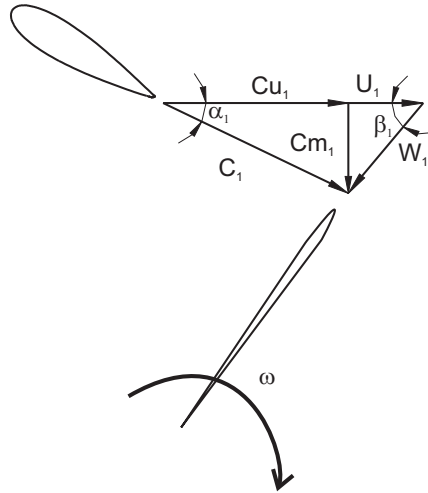


Figure 2.6: Velocity diagram at inlet Francis runner

this thesis has been on the interaction between the wicket gate and the runner. However, some of the most common sources of instability will also be shortly described in the following. For further study on the different topics, it is referred to the textbook by Brennen [13] or PhD-thesis by e.g Stepanik [63], Jernsletten [32], Vekve [68] and Larsson [40].

There are different phenomena that can cause vibrations and pressure pulses through the turbine, some due to the mechanical design and some due to the local condition of the flow. A short outline of the most common sources of vibration and pressure pulses will be given, followed by a review of previous work within the topics with emphasize on pressure pulses at the inlet of the runner. Factors that are important for this thesis' topic will be handled more thorough in section 2.4 on page 15.

The stay vanes might cause vibration due to **vortex shedding** of von Kármán vortices. These vortices have a distinct frequency which can be calculated with the Strouhal formula and empirical values. If this frequencies are in the same range as the natural frequency of the stay vanes, resonance may cause severe vibrations and cracking at the stay vane. The stay vane will also cause a wake which disturbs the flow at the inlet of the guide vanes. Most of the effects caused by the stay vanes will, however, be dampened out before they reach the runner.

Due to their slim profile and thin trailing edge, vortex shedding from the guide vanes will have high frequency and low amplitude, according to [2], and will seldom cause severe problems as long as resonance frequencies are avoided. The main influence from the guide vanes are the viscous wake and the creation of a non uniform flow field in which the runner blades will rotate. As it will be described in the following sections, the severity of this phenomenon is highly dependent of several design parameters. The number of wicket gates and the design of them, the number of runner blades and the distance between the wicket gate and runner are some of the most important parameters and will be described in more details in the following sections.

In the runner, **stall** may occur if the flow have large angles of incidence to the blades. The large incidence angle causes a local eddy at one blade, blocking the main flow and impact on the incidence angle of the nearby blades. Hence the stall will rotate around the runner, so called rotating stall. Stall is very rare in Francis turbines, it is normally found in centrifugal pumps, and pump turbines. The frequency of the rotating stall cell is typically 0.5-0.7 times the rotational frequency of the runner or impeller.

Hydraulic deviations in the waterways or spiral casing can induce a net radial force on the runner. This force can cause a displacement of the runner and produce pressure pulses with a frequency equal to the rotational frequency of the runner [40], [64].

In the draft tube cone and draft tube, **surge** is the main source of pressure pulsations. At off-design conditions swirl flow from the runner will cause varying pressure in the draft tube cone. At part load, this swirl has a shape of a rotating rope, rotating in the same direction as the runner. The frequency of the rotation is the so called Rheingans frequency, approximately 1/3 of the rotational speed of the runner. At full load, the swirl rotates in the opposite direction of the runner and has the shape of a axi-symmetric cavity.

Turbulence and **cavitation** excites a broad band of frequencies with randomly variation, and will therefore not induce any pressure pulses at a certain frequency. Cavitation can, however, under certain condition indirectly cause pressure pulses through a phenomenon called "partial cavitation oscillation." This is more thoroughly described by e.g Brennen, [13, Chapter 8].

2.3 Previous work

A review of previous work within this fields will be presented in following sections. Textbooks within the topic of turbine vibrations are rare, however there are some books for pumps which covers most of the same phenomenons. **Brennen's** [13] book covers hydrodynamics of pumps and most of the topics are valid for turbines as well.

There has been quite a lot of PhD work on this topic. One of them is **Lund** [46] who described the propagation of the pressure pulses in the volute region between the guide vanes and runner by means of Fourier series. With a mathematically expression of the wave propagations, favorable and unfavorable combinations of number of guide vanes and runner vanes have been calculated.

Stepanik [63] focused on improved part load performance in pump turbines. By increasing the number of impeller blades from seven to nine and increasing the blade curvature, part load performances in both pump-mode and turbine-mode have been increased due to more uniform load on the impeller blades. This also caused a reduction of the unsteady pressure fluctuations in the runner.

Jernsletten [32] measured pressure pulses in a model of a Francis turbine runner. Measurements were carried out with pressure transducers on the runner blades, and the results showed a 30% reduction of the pressure pulses on the runner when the distance between the guide vanes and the runner was increased by 5.1 mm.

Larsson [40] investigated the flow field at the inlet of the runner of a Francis turbine in detail. The thesis presented a detailed research of the unsteady inlet flow of a high head Francis pump turbine. The inlet flow field was measured with LDA and pressure pulses between the guide vanes and runner were measured. The results showed that the flow rate in a guide vane passage fluctuates up to 15% of the mean flow due to the influence of the runner blade passages. Both the pressure pulses and the velocity field distinctly changed character when the rotational speed was increased 20 % above the best efficiency point. The measurements also showed that the viscous wake was completely attenuated at the inlet of the runner. Which means that for this turbine, the non-uniform flow field was set up by accelerated flow through the stay and guide vane passage. CFD calculations showed good agreement with the stationary stay and guide vane flow while unsteady calculations, including the runner, deviated somewhat from the measurements.

Antonsen and Nielsen [2] deals with von Kármán vortices in stay vanes in Francis turbines. The paper gives a general extension to the Strouhal formula in order to better predict the frequency of vortices from vanes and slender bodies:

$$f = \text{St} \frac{B}{100} \frac{U}{t + \delta_v} \quad [\text{Hz}] \quad (2.5)$$

Where St is the Strouhal number, U the velocity of the water, B is a shape factor dependent of the trailing edge geometry, t is the thickness of the vane and δ_v is a virtual boundary layer thickness. The paper has been written during the early stages of the work on this thesis and is presented in appendix A.1.

The recent years increase in computer capacity and development of good numerical codes has increased both the amount and complexity of CFD-calculations which is seen by the increasing amount of CFD-papers on the conferences in the latest years. Regarding rotor stator interaction, several papers with different approaches and focuses are presented. An increasing trend is also to include FEM analysis of the materials and to compare all the calculations with experiments. This gives very complete information of the flow and load on the turbines and is also a good opportunity to validate the numerical code. Generally it is

quite good agreement between calculations and experiments, given that enough effort is made in order to create a fine enough mesh and take the cost of long calculation time.

Ruprecht et al [59] carried out a numerical calculations of a complete Francis turbine, including spiral case, stay vanes, guide vanes, runner and draft tube. The motivation for this was to avoid simplifications and periodic assumptions. This resulted in a huge mesh size and very costly in terms of computer time.

Also **Page et al** [54] compute transient rotor stator interaction by modeling the whole turbine from spiral case to draft tube. The use of large eddy simulation (LES), gave quite good results compared with experiments.

Segoufin et al [61] did a comprehensive analysis of unsteadiness in a high head pump turbine. Calculations including a 3D-model of the whole runner, wicket gate and stay vanes were carried out together with a simplified 2D calculation. Calculating the fluctuations at the guide vanes and runner blades, the results showed that the 2D calculations only varied about 6% from the 3D calculations which opens for a tremendous saving in computational time, using 2D instead of 3D. While a complete 3D calculation require CPU-time in means of weeks, the 2D calculations can be carried out in hours.

An interesting fact, presented by **Zobeiri et al** [79] shows that the pressure actually will fluctuate all the way upstream the stay vanes due to the passing of a runner blade. This is in agreement with the measurements carried out by Larsson [40].

Even though a calculation of the whole turbine geometry gives valuable information, the time aspect makes this kind of calculations poor fitted for industrial use. A paper presented by **Nennemann et al** [48] describes how GE Energy uses CFD in turbine design. By comparing numerical calculations with experiments, a way to simplify the calculations was found. If the ratio between the area of stationary and rotating interfaces lies between 0.99-1.01, the simplification gives negligible impact on the results. For example a case with 24 guide vanes and 17 runner blades can be reduced to 7 wicket gates and 5 runner blades with an area ratio of 0.99167. This will significantly reduce the mesh size and save calculation time.

As it just have been shown; lots of work have been carried out in order to investigate the interaction between the wicket gate and the runner. The flow field is complex and highly time dependent. Also the design of each turbine will affect the flow, since a pump turbine with, say, 8 runner blades will have quite

a different 'interaction pattern' than a high head turbine with, say, 24 runner blades (including splitter blades). This makes it difficult to draw out general guide lines to cover all different cases. Some rules of thumb are acknowledged as important and general guide lines, e.g the ratio between the number of guide vanes and runner blades, and the distance between the outlet of the guide vanes and inlet of the runner blades. However, the design of the guide vanes in order to reduce the dynamic load on the runner is seldom discussed. In the following sections the rotor/stator interaction phenomena will be presented in more detail and also how the design of the wicket gate can contribute to reduce the dynamic load on the runner. The presented hypothesis are based upon fundamental fluid theory, and a short introduction of topics of current interest will be given.

2.4 Wake flow

The first approaches to the theory of fluid dynamics assumed perfect, frictionless fluid behavior. Euler developed both the differential equations of motion and their integrated form, now called the Bernoulli equation. D' Alembert used these equations to show his famous paradox; that a body immersed in a frictionless flow has zero drag. After Navier and Stokes successfully added the viscous terms to the equations of motion and Prandtl introduced the boundary layer theory, calculations on real flow could be carried out [74].

Any body in a 'real', viscous flow will have a drag force and lift force caused by the local acceleration of the flow over the wing and also create a wake in the flow downstream the body. On a wing profile the drag and lift will be as shown in figure 2.7 on the following page. A blunt body, as e.g a circular cylinder, will have a quite broad and pulsating wake due to the flow separation. Slender bodies such as a wing or a guide vane will have a much narrower wake, but even for such bodies the wake flow is quite complex. The wake will gradually mix out due to mixing with the flow in the free stream. The flow in a wake consists of free shear flow with high Reynolds number in an ambient fluid. Since there is no influence from walls or surrounding bodies, the flow is often described as *free turbulence*. Since the flow is "free" or unconfined, the pressure through the wake is approximately constant throughout the flow, except for small turbulence fluctuations [73].

Wake flow will consist of different zones. Close to the trailing edge, it will be a dead water region, followed by a mixing zone before the pure wake flow is

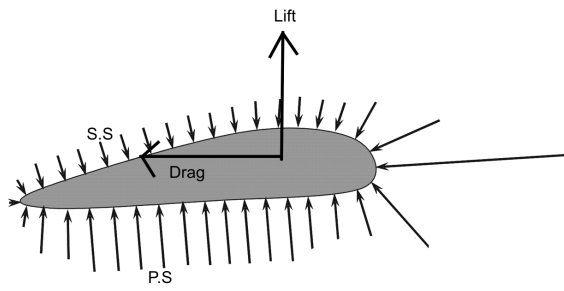


Figure 2.7: Lift and drag force on a wing profile

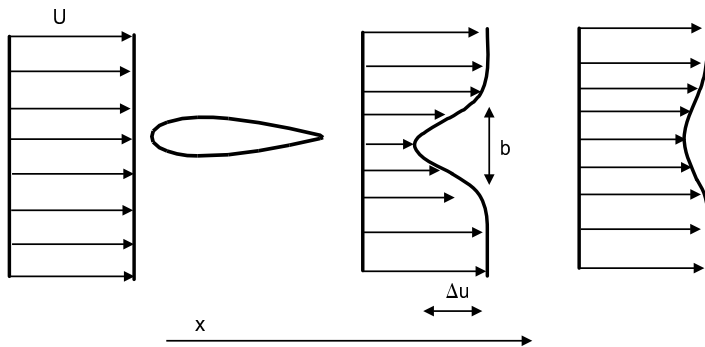


Figure 2.8: Wake behind a body

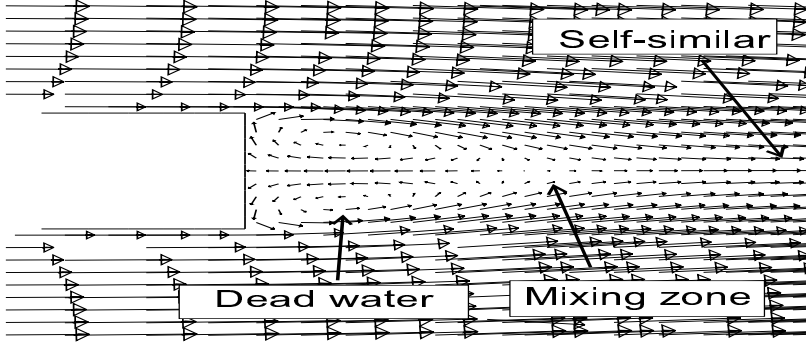


Figure 2.9: Regions in wake flow, CFD plot from [1]

established. The size of the dead water zone is dependent of the shape of the trailing edge. Slender and aerodynamic bodies will have a smaller zone than a blunt body. In the mixing zone, momentum is transferred between the wake flow and the free stream. When pure wake flow is achieved, the velocity profile will have a self preserving shape, and so called self-similarity is achieved. According to White [73], the drag force, F , within a plane wake can be expressed as:

$$F = \int_{-\infty}^{\infty} \rho \bar{u} \Delta u dA \approx (\text{const}) \rho U \Delta u_{\max} b \quad [\text{N}] \quad (2.6)$$

By assuming a small defect, $\Delta u \ll U$ and $u(\partial u / \partial x) \approx U(\partial u / \partial x)$ and substitute this assumptions into the boundary layer equations, it comes forth that similarity cannot be achieved unless:

$$\Delta u = \text{const} \cdot x^{-1/2} \quad (2.7)$$

$$b = \text{const} \cdot x^{1/2} \quad (2.8)$$

Since the wake flow consists of large-scale structures dependent of the body shape, e.g Kármán vortex street, it is difficult to establish general constants for equations (2.7) and (2.8). The constants must therefore be determined by experiments on a case by case basis. Kjeldsen et al [38] found that self similarity of the wake shapes exist quite close to the trailing edge ($x/c = 0.12$, where c is the chord length).

As the previous pages concluded, the flow field downstream the wicket gate consists of a blade-to-blade pressure difference, both due to the accelerated flow field and the local pressure and suction side of the vanes. In addition, the viscous wake will create a velocity defect, affecting the velocity distribution. The runner blades will also have a blade-to-blade pressure difference and due to the rotation of the runner, this pressure difference will rotate with the runner. In addition to this, the stagnation point at the leading edge of the runner blades will also rotate with the runner. Every pressure wave created will travel around the circumference with the speed of sound until it is dampened out. Together this will cause a complicated pressure field in the region between the outlet of the wicket gate and inlet of the runner. However, the pressure propagation can be described by means of Fourier series e.g as suggested by Nicolet et al. [50] or Lund [46]. A far more easy and strait forward approach can be used to visualize the phenomenon: Imagine a pressure pulse created each time a runner blade passing a guide vane, traveling around the circumference with the speed of sound. Amplifications of the pressure pulses may occur if the combination of number of guide vanes and number of runner blades is unfavorable. If the number of guide vanes and runner blades have a common factor, more than one blade will hit a wake at the same time. With e.g. 24 guide vanes and 30 runner blades, 6 runner blades are passing 6 guide vanes simultaneously while 5 blades in front of each blade are passing wakes before the regarded blade is passing the next guide vane wake. As a result, 5 pressure pulsations are entering the runner in-between each blade passing frequency of a regarding blade.

Amplification may also occur if the shock propagation speed from one blade passing pulse reaches the next guide vane wake at the same time as the blade in front of the regarding blade is passing the wake. This situation occur if the number of runner blades is higher than the number of guide vanes. If the number of guide vanes is higher than the number of runner blades, the shock wave will travel in the opposite direction.

The time for the shock wave to travel the distance between two guide vanes will be as shown in figure 2.10. The velocities are defined in the velocity diagram in figure 2.6 on page 10.

$$\Delta t_{GV} = \frac{\pi D}{(a + c_u)Z_g} \quad [\text{s}] \quad (2.9)$$

The time for the nearest runner blade in front of the regarded blade to reach

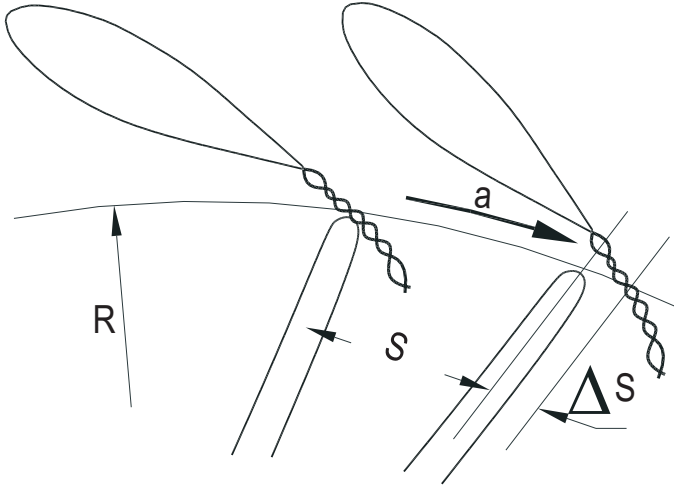


Figure 2.10: Wave and runner propagation

the next guide vane wake by constant runner speed will be:

$$\Delta t_r = \left(\frac{\pi D}{Z_g} - \frac{\pi D}{Z_r} \right) \frac{1}{\omega D/2} = \frac{(Z_r - Z_g) 2\pi}{Z_r Z_g \omega} \quad [\text{s}] \quad (2.10)$$

Interference will occur if $\Delta t_g = \Delta t_r$, i.e.

$$\frac{Z_r - Z_{GV}}{Z_r} = \frac{\omega D/2}{a + c_u} \quad [-] \quad (2.11)$$

If the number of guide vanes is higher than the number of runner blades, the formula yields:

$$\frac{Z_{GV} - Z_r}{Z_{GV}} = \frac{\omega D/2}{a - c_u} \quad [-] \quad (2.12)$$

It is important to keep track of the different frames of references in a system consisting of both a rotating and a stationary part. For a runner blade in a rotating frame of reference, the main frequency due to RSI will be:

$$f_r = \frac{nZ_g}{60} \quad [\text{Hz}] \quad (2.13)$$

For a stationary point, the corresponding frequency will be:

$$f_{GV} = \frac{nZ_r}{60} \quad [\text{Hz}] \quad (2.14)$$

Chapter 3

Numerical model

In order to test the hypothesis, a series of CFD-calculations have been carried out. Pressure distribution downstream guide vanes with different profiling have been calculated and compared. Also the velocity defect in the wakes has been calculated as a factor suitable for comparison with experimental data. The commercial program *Fluent 6.2.16* with *Gambit 2.2.30* as a preprocessor has been used for all the calculations.

3.1 Model details

According to experience, it has been assumed that a simplified model consisting of three stay vanes and three guide vanes in a periodic, 2-dimensional domain would be sufficient for this kind of calculations. The calculation area is shown in figure 3.1 on the following page. The inlet was located a chord length upstream the stay vanes in order to let the flow field to be fully developed at the inlet of the stay vanes. The outlet was located a chord length downstream the point of where the inlet of the runner would be. Inlet boundary condition was *velocity inlet*, set as velocity components in x and y direction. The inlet velocity was equal to the velocity used in the experiment, see chapter 4 on page 33, and the flow angle was set to match the inlet angle of the stay vanes and guide vanes. *Outflow* boundary condition has been used at the outlet. This condition requires

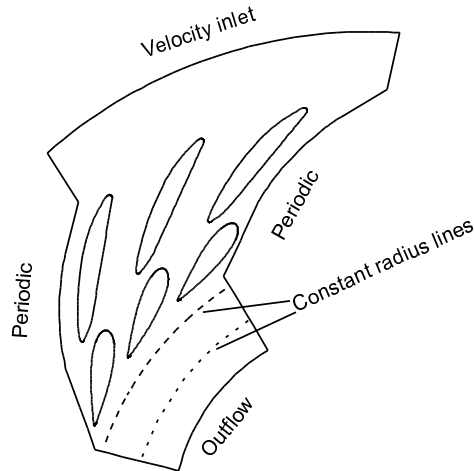


Figure 3.1: Calculation area

no initial values since Fluent extrapolates the required information from the interior.

A *quad-pave* type mesh, which is an unstructured quadrilateral mesh has been used for all the calculations. This mesh type gives the flexibility of a unstructured mesh but also the structured mesh's benefit of using aspect ratios. Around the vanes, the boundary layer function has been used to create a structured grid close to the vane walls. This function makes it is possible to control that the boundary layer is proper resolved by placing the grid cells close enough to the wall according to the requirement of the chosen turbulence model. An example of mesh around a guide vane is shown in figure 3.2 The size and quality of the mesh will of course influence the results. Some important factors that determines the grid quality are: enough cells to describe the geometry correct and enough cells to resolve gradients in the flow. The quality is based on the skewness and aspect ratio of the mesh cells. The aspect ratio is a measure of the cell stretching, and should not be larger than 1:5 at maximum [23]. The skewness is the difference of the shape of a cell compared with a equilateral cell with the same volume. In Gambit, the quality of the skewness and aspect ratio can be visually controlled by the *examine mesh* function, which was used

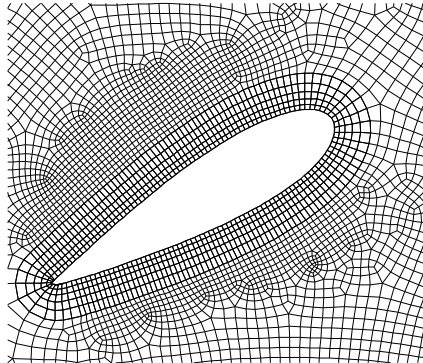


Figure 3.2: Mesh around one guide vane

for all the calculations. To ensure proper resolution of the boundary layer the parameter, y^+ has been used. y^+ is the dimensionless distance from the wall, defined in equation (3.1):

$$y^+ = \frac{u_\tau y}{\nu} \quad [-] \quad (3.1)$$

To calculate the real distance from the wall, the friction velocity must be calculated. This velocity, u_τ , is defined as¹:

$$u_\tau = \sqrt{\frac{\tau_w}{\rho}} \quad [\text{m/s}] \quad (3.2)$$

It is not easy to calculate an exact value of u_τ but it can be estimated using the integral momentum equation, defined in equation (3.3):

$$\frac{\tau_w}{\rho U_e^2} = \frac{C_f}{2} \quad [-] \quad (3.3)$$

The skin friction coefficient, C_f , can either be estimated from a flat plate correlation or by special airfoil software as e.g *XFOIL* [75]. It turns out that the flat plate estimation gives negligible difference from the more exact *XFOIL* solution. Finally, the distance from the wall can be calculated by equation (3.4),

¹Some literature denotes the friction velocity as u^*

by estimating the skin friction coefficient and choosing an appropriate value of y^+ :

$$y = \frac{y^+ \nu}{u_\tau} = \frac{y^+ \nu}{\sqrt{\frac{C_f U_\infty^2}{2}}} \quad [\text{m}] \quad (3.4)$$

The importance of creating the mesh at correct distance from the wall is due to the wall and the boundary layer's influence on the turbulent flow. Both the physical wall and the boundary layer, in which the viscous forces are dominant, will dampen out the turbulent fluctuations. The turbulence models are only valid in 'free stream turbulent flow'. Figure 3.3 on the facing page shows the three layers of the flow; the viscous inner layer, the overlap layer and the outer layer, in which the wall law is valid. To ensure that the boundary layer is properly resolved, the y^+ value is set according to the recommended values in the Fluent manual [23], and as shown in figure 3.3, between 30-300, dependent of the mesh size and choice of turbulence model.

In Fluent, there are two different approaches to modeling the two inner regions. Either by *wall functions* or *near wall modeling*. The wall function uses semi-empirical formulas as a 'bridge' between the two inner layers and the fully turbulent region. The near wall approach modifies the turbulence models to be valid all the way down to the wall. If this approach is used, the mesh must be created with $y^+ < 5$.

The meshing strategy was first to calculate an appropriate distance from the wall to place the first mesh cell, thereafter a mesh was generated according to experience and the guidelines from the Fluent manual. The mesh was then refined until the results from the calculations did not change. Then the mesh was coarsened as much as possible until the results was changed. By this iteration it was ensured that a mesh-independent solution was found and still reduce the mesh size, and hence the computer time, as much as possible.

The calculations were considered converged when the residuals reached a constant value. According to the Fluent manual [23], a residual value of 10^{-3} is sufficient and for standard computers, any value below 10^{-5} will be rounding errors in the computer system. The convergence of lift and drag force is also used to determine the convergence, together with the mass balance between inlet and outlet. The mass flow is calculated at inlet and outlet and should be equal if the calculations are perfectly correct. Large differences in the mass flow indicates numerical inaccuracy, but in all cases the differences were in a order of magnitude of 10^{-5} , which indicates an accurate solution.

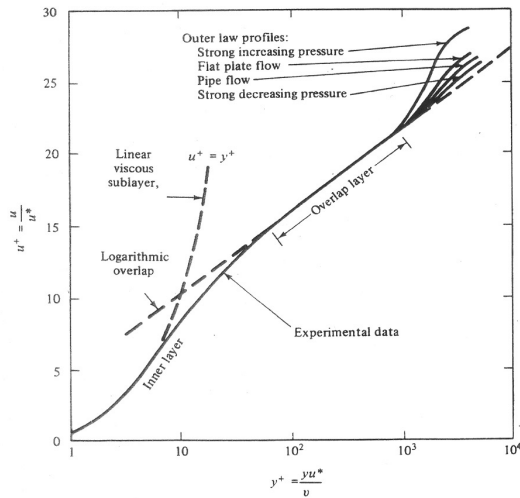


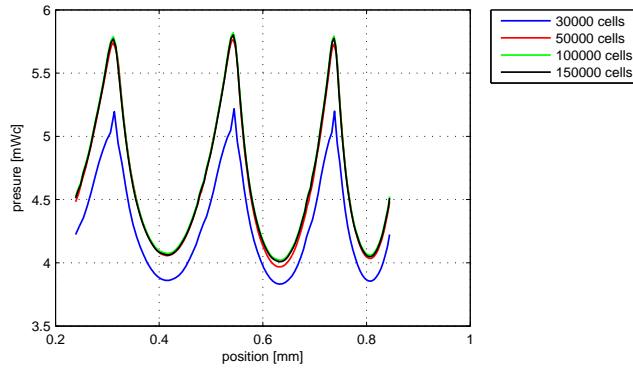
Figure 3.3: The different layers in the near wall region, from [74]

3.2 Results

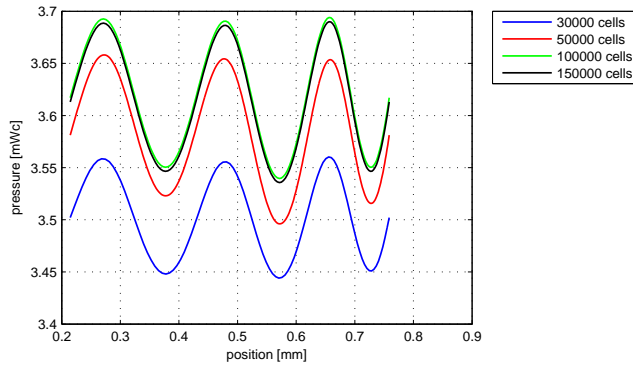
3.2.1 Mesh dependency

Figure 3.4 and 3.5 shows the pressure and velocity as a function of the mesh size. The x-axis describes the position along the constant radius lines shown in figure 3.1.

It can be seen that the pressure right downstream the trailing edge is not very sensitive of the mesh size, but at some distance further downstream the results show much more dependency of the mesh size. This is probably due to the fact that the flow right downstream the trailing edge is dominated by the flow field past the guide vanes and the pressure difference is 'forced' upon the flow due to the acceleration. Further downstream the pressure will mix out due to the diffusion, and since this is a process within the water it selves, it will be more dependent of the mesh size, since this describes the spatial 'resolution' of the water.

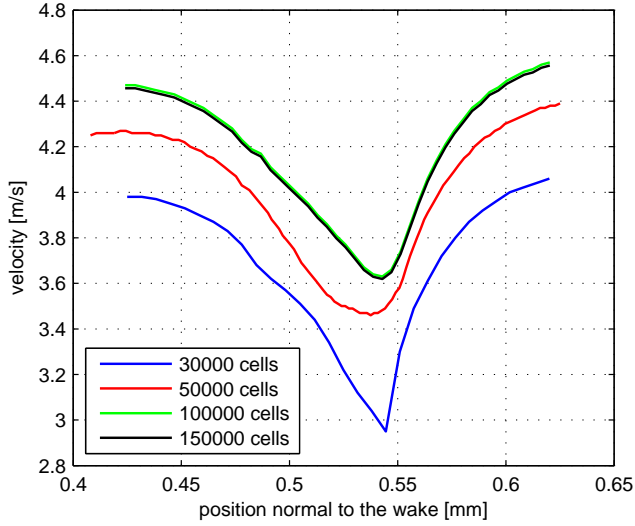


(a) Pressure distribution at the outlet of the guide vanes

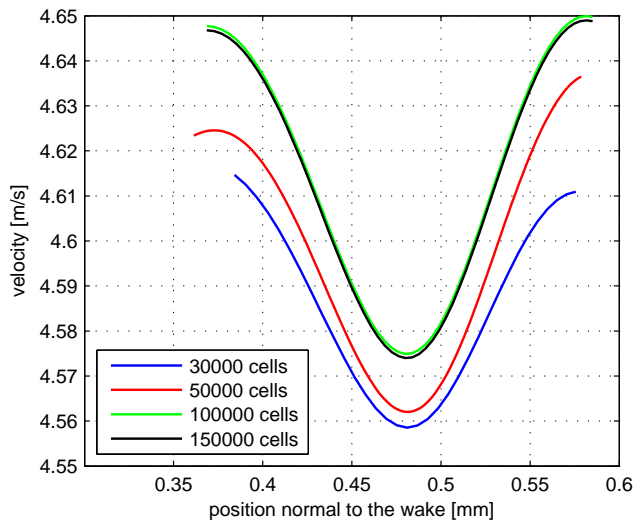


(b) Pressure distribution at the inlet of the runner

Figure 3.4: Pressure distribution vs. mesh size



(a) Wake at the outlet of the guide vanes



(b) Wake at the inlet of the runner

Figure 3.5: Wake vs. mesh size

3.2.2 Turbulence model dependency

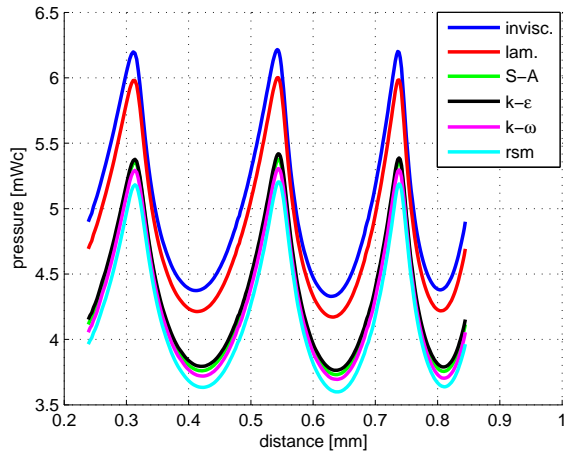
The $k - \varepsilon$ turbulence model has been used since this is the simplest of the 'complete models' and, hence, the less costly in terms of computational time. The model assumes that the flow is fully turbulent and that the effect of the molecular viscosity is negligible. The model is well known and well developed, with good accuracy for a wide range of turbulent flows. The standard model has been improved as its weaknesses has been derived throughout the years. In Fluent, two variants of the standard model is available: The RNG-model and the realizable-model. The standard model has been used in this thesis. For comparison, the different models in Fluent have been used. Especially the one-equation model, Spalart-Allmaras, is of interest since this model was designed specifically for the wing profiles and aerospace applications and are built to use meshes that resolve the viscous regions. This means that the model should have a mesh similar to the $k - \varepsilon$ model with enhanced wall treatment. Being a one-equation model the calculation time will be shorter than for the two-equation $k - \varepsilon$ model. Figure 3.6 show the pressure distribution and the velocity wake for calculations with different turbulence models.

As the figure shows, there are small differences between the different turbulence models, while the laminar and inviscid solutions differ from the other solutions. As expected, these models show a less dampened flow and a flow with less losses than the turbulent cases. It can also be seen that the pressure distribution is not very dependent on the viscosity, since even the inviscous solution shows a distinct variation in the pressure. Naturally, there are relatively larger differences in the wake since this is more dependent of the viscosity.

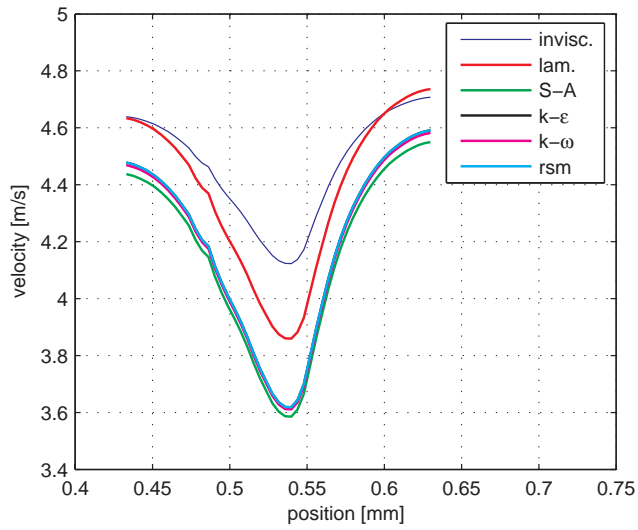
3.2.3 Pressure distribution

Four different guide vane profiles have been calculated in order to see what influence the profile has on the pressure distribution. One symmetric, one slightly asymmetric the 'correct' way ('flat side' toward the runner), and two more extreme asymmetric profiles, both on the 'correct' side and 'wrong' side, see figure 3.9 on page 31. The pressure distribution at the outlet of the guide vanes for the different profiles is shown in figure 3.7 on page 30 and figure 3.8 on page 30 shows the pressure distribution at the inlet of the runner.

It is clear that the profiling of the guide vanes does impact the pressure distribution, according to the hypothesis. With the pressure side of the guide



(a) Pressure distribution with different turbulence models



(b) Wake with different turbulence models

Figure 3.6: Results from different turbulence models

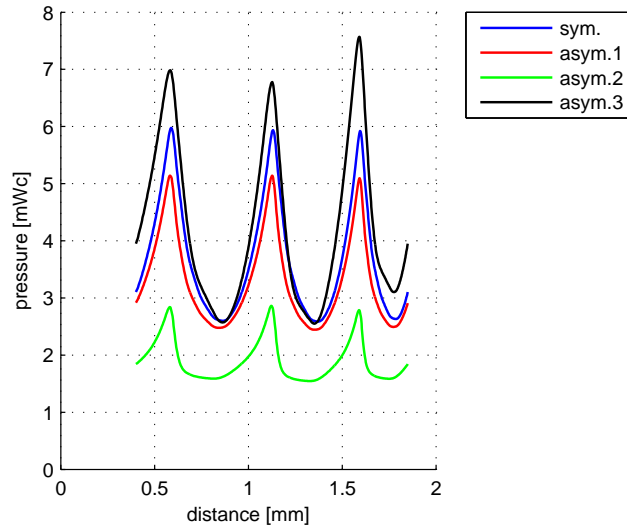


Figure 3.7: Pressure distribution outlet GV with different guide vane profiles

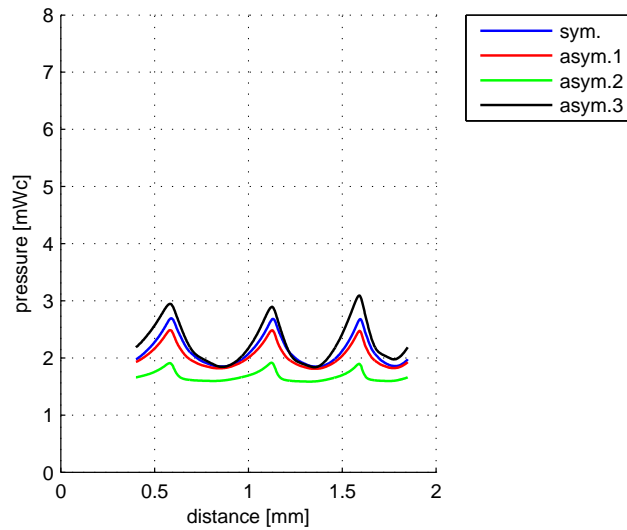


Figure 3.8: Pressure distribution inlet runner with different guide vane profiles

vane counteracting the pressure difference from the accelerating flow, the overall pressure distribution will be more uniform. It is also clear that the pressure difference gradually will mix out, giving a more uniform distribution at the runner inlet than at the trailing edge of the wicket gate, but even at this position, there are still differences between the different profiles.

Before any further calculations were carried out, LDA-measurements were carried out in order to validate the numerical code.

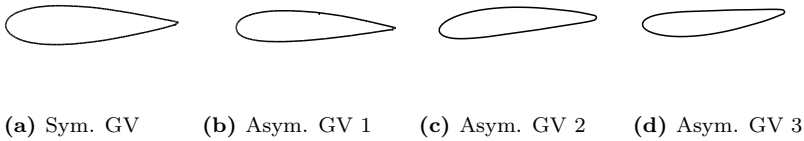


Figure 3.9: GV profiles

Chapter 4

Experiment

In order to verify the CFD-calculations and gain more information for this kind of flow field, a measurement series has been carried out. This chapter will present the setup for the test rigs, describe the different techniques and details about the equipment. The velocity distribution in the wake downstream the guide vanes have been measured using the LDA-technique, while hollow guide vanes have made it possible to measure the pressure distribution around the guide vane profile with a pressure transducer. The results have been used as a comparison to the CFD-calculation, and will be presented in section 4.2.

A test series with dynamic pressure pulse measurements in a Francis model turbine has also been carried out. Pressure transducers mounted in the lower cover in the volute region between the outlet of the wicket gate and the inlet of the runner have been used in order to measure the fluctuating pressure. Since this measures the load on the wicket gate from the runner, and not the load on the runner from the wicket gate, this measurements are omitted from the main part of this thesis and are presented in appendix A.3, as a paper submitted to the 23th IAHR symposium.

4.1 Experimental set-up

4.1.1 LDA principles and rig setup

For the velocity-measurement, a test rig with five stay vanes and five guide vanes has been used. This rig was originally built as a part of Chen's PhD-thesis [14], but was convenient to use for this project as well. The rig is a double cascade with symmetry around the middle Guide vane. In order to obtain this symmetry, a guidance wall has been mounted at the inner curve of the bend. The facing plates were 30 mm thick, made of plexiglass in order to perform LDA-measurements. The rig is a 0.40 scaled homologous model of the last quarter of the spiral case of a high head Francis turbine with $H_n = 543$ m. A sketch and a picture of the rig is shown in figure 4.1.

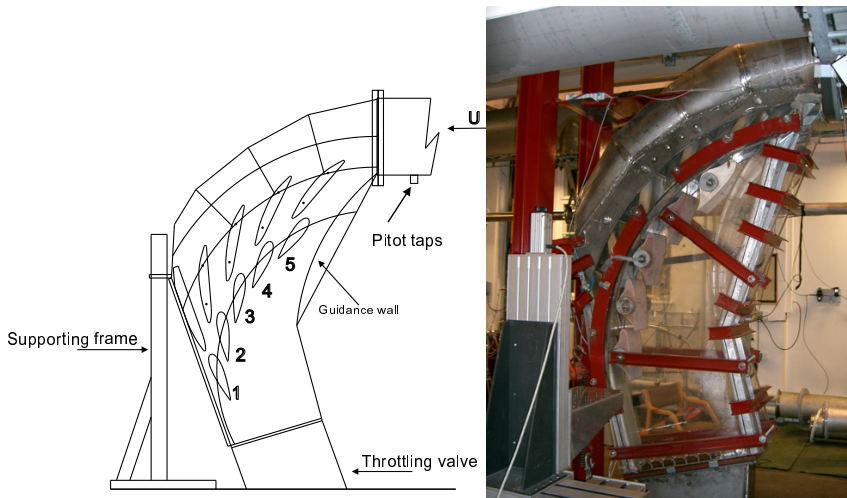


Figure 4.1: The cascade rig

Laser Doppler Anemometry, LDA, is well suited for this kind of measurements, due to its non-intrusive nature, high spatial resolution, and since there is no need to calibrate the equipment. The principles of LDA are well described in several textbooks, e.g. Drain [19], Goldstein [25] and Durst [21], therefore only a short outline will be given here.

Figure 4.2a on the next page summarizes the principles of the differential Doppler mode, which have been used for the measurements in this thesis. The main principle is to focus two laser beams in a small volume, in which the velocity is measured. Particles in the flow reflect the light from the lasers and the Doppler shift of this light is proportional with the velocity of the particles. It is assumed that the velocity of the particles is the same as the velocity of the flow, which is a reasonable assumption.

The laser beam is split into two beams by a Bragg cell. The two beams intersect with a certain angle, θ , and due to the interference, a fringe pattern as shown in figure 4.2b will be created. The distance between the interference fringes, d_f is constant, given by the wavelength, λ , and the angle, θ , between the two beams. From figure 4.2b it can be seen that the fringe spacing is given by:

$$d_f = \frac{\lambda}{2 \sin(\frac{\theta}{2})} \quad [\text{mm}] \quad (4.1)$$

A particle passing through the fringe pattern will reflect light from both the laser beams. Since the beams are at an angle of each other, the reflections will have different Doppler shifts. The interference of these two shifts produce a pulse in the light intensity, which can be measured by the photo detector. The frequency of this pulsation, f_D , is proportional to the velocity component perpendicular to the fringe pattern. Hence the velocity component can be calculated by equation (4.2).

$$f_D = \frac{u_x}{d_f} = \frac{2u_x \sin(\frac{\theta}{2})}{\lambda} \quad [\text{Hz}] \quad (4.2)$$

One pair of laser beams are needed per velocity component. In this thesis, two components have been measured with a 300 mW Ar-ion laser from TSI. The focal length of the probe was 350 mm in air, further details are presented in table 4.1.

The LDA probe has been traversed in three directions by a traverse table, governed by a computer. A sketch of the rig set-up is shown in figure 4.3 on page 37 and pictures from a measurement series is shown in figure 4.4. Polyamid seeding particles, non-spherical but round, with a mean particle diameter of 5 μm and density 1030 kg/m^3 have been added to the water in order to increase the sample rate. The probe has been traversed with small steps, typically ca 0.5 mm in the wake region and slightly coarser steps in the free stream. It has been acquired 5000 valid samples in each measurement point, filtered with a

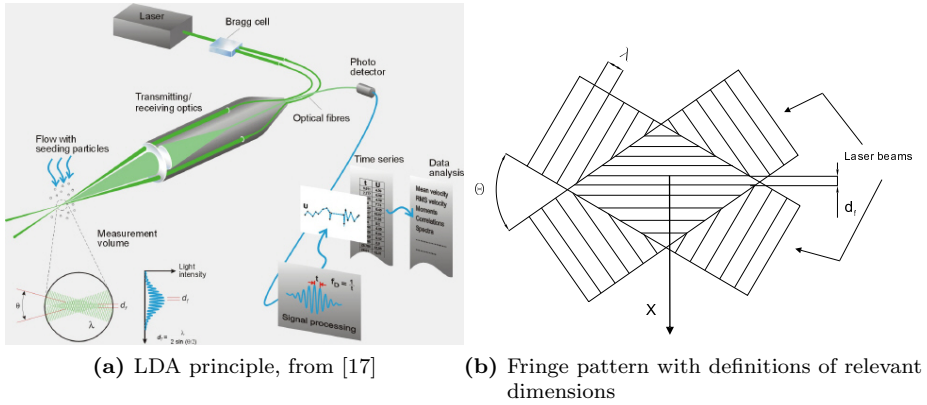


Figure 4.2: LDA principles

Color	Unit	Green	Blue
Beam Separation	mm	50	50
Wave length, λ	nm	514.5	488.0
Fringe spacing	μm	3.41	3.24
Diameter of measuring vol.	mm	0.10	0.10
Length of measuring vol.	mm	1.45	1.37
No. of fringes		32	32

Table 4.1: LDA Characteristics (in water)

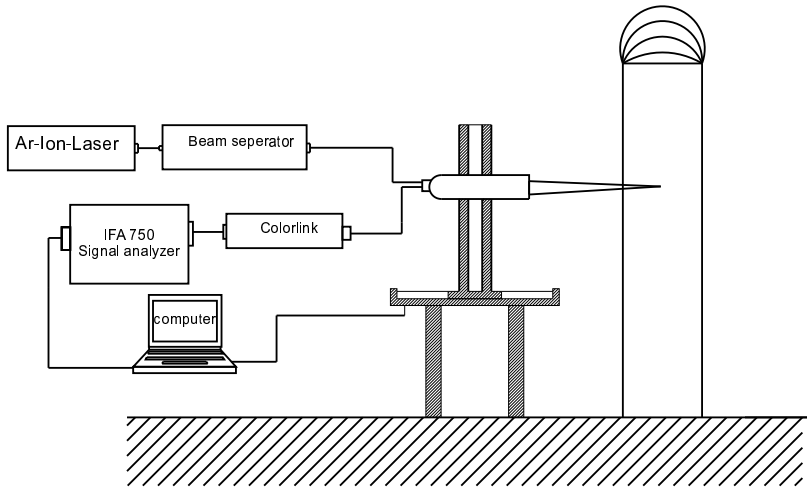


Figure 4.3: LDA set-up

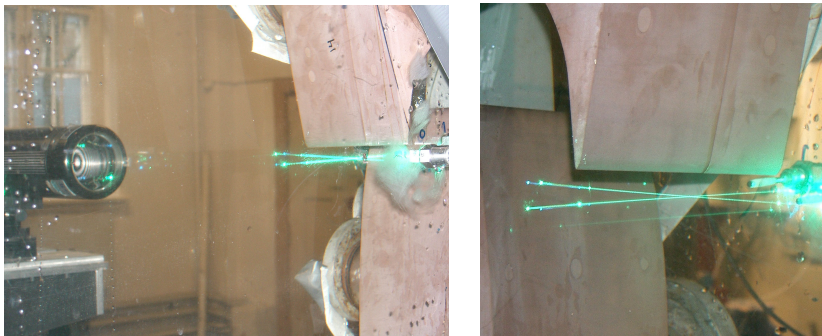


Figure 4.4: LDA measurements

coincidence window which means that the software only accept signals when the two components are measured simultaneously within a given time window. According to the TSI-manuals [66], this window have been set to the inverse of the sample rate, typically 10^4 ms for most of the measurements.

The Find software provided a post processing routine from which the mean velocity, variance and turbulence intensity have been calculated using the following formulas:

$$\bar{u} = \frac{1}{N} \sum_{i=1}^N u_i \quad (4.3)$$

$$\sigma^2 = \frac{1}{N} \sum_{i=1}^N (u_i - \bar{u})^2 \quad (4.4)$$

$$\text{Tu} = \frac{\sigma}{\bar{u}} \cdot 100\% \quad (4.5)$$

Where N is the number of valid samples. The following parameters have been varied during the tests:

- Two different guide vane profiles
- Two different guide vane angles, α
- Three different flow rates, Q
- Different downstream positions
- Different span-wise positions

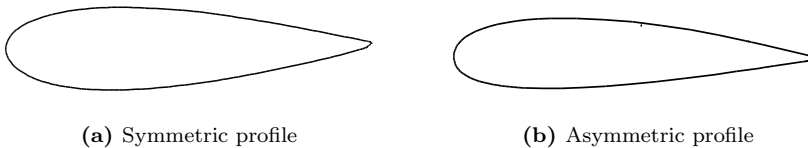


Figure 4.5: Guide vane profiles

The profile of the two guide vanes is shown in figure 4.5. The guide vane in figure 4.5a is a symmetric profile with chord length 335 mm. The guide vane in figure 4.5b is slightly asymmetric with a chord length of 325 mm. Both profiles

are examples of typically guide vane profiles, provided by the courtesy of GE Energy.

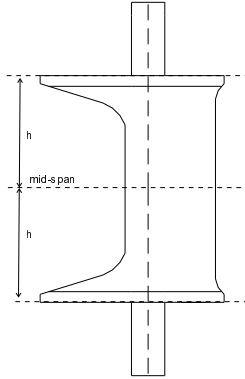


Figure 4.6: Vertical view of the guide vane profile

4.1.2 Flow measurement

Unfortunately, the chosen test loop did not contain any flow meters, therefore the flow rate has been calculated by pitot measurement in the inlet pipe. By measuring the velocity through the diameter of the pipe, the flow has been calculated using equation (4.6):

$$Q = \int U dA = \int_{-R}^R u(r) 2\pi r dr \quad [\text{m}^3/\text{s}] \quad (4.6)$$

4 entrance holes have been made, 45° on the centerline and 90° on each other, see figure 4.7. The pitot probe covered 65 % of the pipe diameter and has been traversed from all four holes, covering the whole diameter by good margin.

4.1.3 Guide vane pressure-profile

The middle guide vane for both profiles have been made hollow and instrumented with pressure taps around the whole profile in order to measure the pressure

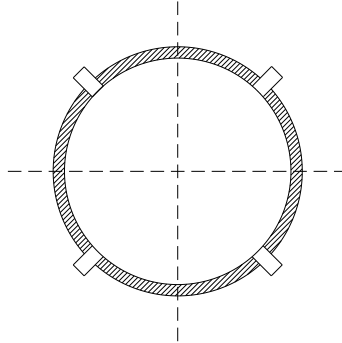


Figure 4.7: Pitot taps at the inlet pipe

distribution around the profile. Figure 4.8 shows a principle sketch of the guide vane and the placing of the 14 pressure taps. The placing of the taps near the trailing edge has been limited by the thickness of the guide vane. Soft tubes have been connected to the pressure taps and connected to a pressure transducer via a Scanivalve 45J7-677 multichannel valve. With this valve it has been possible to measure the pressure from all 14 points with only one transducer. The valve opens one channel at the time, measuring the pressure in steps, not simultaneously. This requires an assumption for steady pressure, which in this case was a reasonable assumption. A Kulite HKM-375 piezoresistive transducer has been used, calibrated to gauge pressure. All the pressure data have been sampled into a PC with a self developed program in LabView and saved to disk for further post processing and analysis.

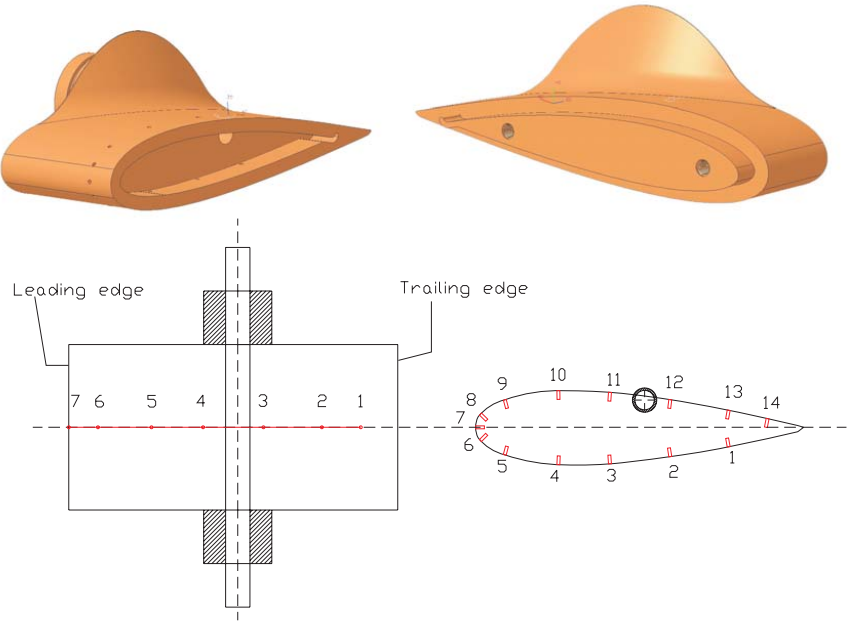


Figure 4.8: Instrumented guide vane

4.2 Experimental results

Figure 4.9 shows a velocity profile from the pitot measurements. As seen from

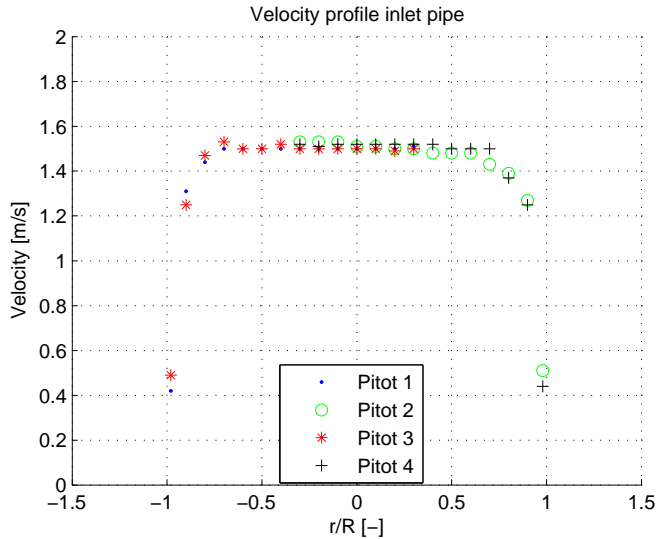


Figure 4.9: Velocity from pitot measurements

the figure, the profile is a typical turbulent pipe velocity profile, without vortices or back-flow. The volume flow has been calculated by solving equation (4.6) numerically. The overlapping measurements compares very good, which is a quality statement to the measurements. In the overlapping region, the mean of the four values have been used in the calculations.

It have been experienced some leakage problems with the cascade rig. Therefore, the rig was pressurized with care. This also limited the the maximum flow rate used in the experiments. It turned out that the pressure had to be adjusted with some care to give optimum measurement conditions. Too high pressure gave a rather high rate of leakage and too low pressure gave cavitation and air bubbles in the flow, which made the LDA measurements difficult. The pressure was regulated by the throttle valve at the exit of the cascade. This limitation made it difficult to run the test rig with similar Reynolds number as the prototype. However, an average Reynolds number based upon the chord

length of the guide vane is of order of magnitude $2.5 \cdot 10^6$ while for the prototype, the average Reynolds number is of order of magnitude $4.5 \cdot 10^6$. This is assumed to be close enough for the purpose of the work within this thesis since there are no direct comparison between measurements on the prototype and on the model. The comparisons in this thesis are between the model test and CFD-calculations which have the same Reynolds number.

The maximum changes in the water temperature for all the experiments have been 5°C , ($19\text{-}24^\circ\text{C}$). According to table B.3 in the IEC standard [29] this gives a variation in kinematic viscosity on $1.16 \cdot 10^{-7}\text{m}^2/\text{s}$, which has assumed not to influence on the results.

Since the main focus has been the influence of the guide vane profile on the flow field, the major part of the measurements have been carried out at mid-span of the guide vane. According to Chen [14], the flow at the mid-span is the most undisturbed flow since the influence of leakage flow and boundary layer of the facing plates are negligible at this position.

As mentioned, it has been measured with two different sets of guide vanes. The first set has been measured with three different flow rates and two different guide vane angles. During assembling of the new set of guide vanes, the fastening bolt on one of the vanes broke. This required the vane to be welded to the rig in order to be kept in place. Because of this it has not been possible to change the guide vane angle of the new set of vanes. Therefore, only changes in flow rate have been carried out with this set. It has been measured in different downstream positions. Due to the angle of the laser beams, the point closest to the trailing edge possible to measure at mid-span is located about 11 mm from the trailing edge.

In the following sections, some abbreviations have been used for simplifications in captions and labels. An overview of these abbreviations are given in table 4.2.

The test matrix for the measurements is shown in table 4.3. The pressure around the guide vane profile has been measured for each of the cases in the test matrix. First the velocity was measured in the free stream in span wise direction to confirm that the flow field was uniform, without vortices or back-flow. As shown in figure 4.10 on page 45, the flow is quite uniform in this direction. These measurements have rather coarse steps and is conducted to see if any large flow structures disturbs the mean flow at mid span. As measured by Chen [14], influence from the boundary layer of the facing plates and horseshoe

GV1	symmetric guide vane profile
GV2	asymmetric guide vane profile
$\alpha 1$	10.5 °
$\alpha 2$	5.0 °
Q1	0.268 m ³ /s
Q2	0.346 m ³ /s
Q3	0.402 m ³ /s
Q4	0.290 m ³ /s

Table 4.2: Abbreviations

Guide Vane	α	Flow
1	$\alpha 1$	Q1, Q2, Q3
1	$\alpha 2$	Q4, Q2
2	$\alpha 1$	Q2, Q4

Table 4.3: Test matrix for guide vane measurements

vortices will affect the flow, but at the mid span this influence is negligible.

4.2.1 Guide vane pressure-profile

Figure 4.11 on page 47 shows the results from the pressure measurements around the guide vane profile. The placing of the pressure taps are defined in figure 4.8. The results are presented as the dimensionless pressure coefficient, C_p , as a function of the dimensionless distance x/c , where x is the distance from the leading edge, c the chord length and C_p as defined in equation (4.7):

$$C_p = \frac{P - P_{\text{ref}}}{\frac{1}{2}\rho U_{\infty}^2} \quad [-] \quad (4.7)$$

Where U_{∞} is the free stream velocity, found from the LDA-measurements, and P_{ref} is a reference pressure. According to the definition of C_p this is the pressure in the free stream, but in this case the pressure in the inlet pipe is used. This because of the lack of suitable pressure taps in the free stream in the cascade. The pressure in the inlet pipe is, however, proportional to the pressure in the cascade so it is applicable for comparing the different test series, but the absolute value of C_p might differ from other experiments.

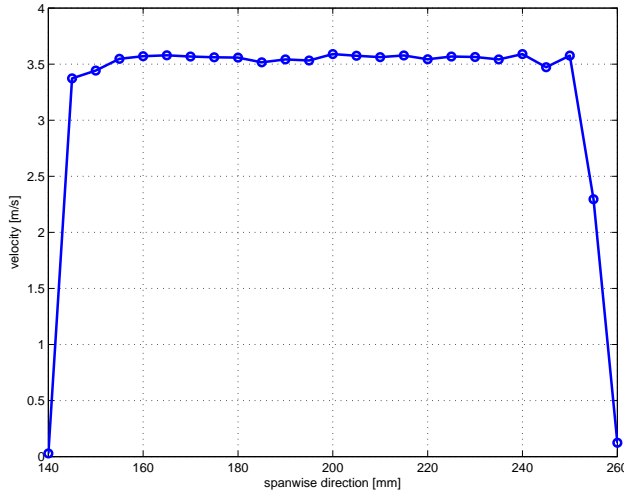


Figure 4.10: Spanwise velocity profile

The results from the pressure measurements show good agreement with the expected results. The pressure is highest at the stagnation point and is gradually lower down the sides as the flow is accelerated. At the trailing edge there is a pressure difference due to the difference between the pressure side and the suction side of the guide vane. It seems that the use of the inlet pipe pressure for normalization might not be appropriate for direct comparison of the results. Hence it should be emphasized to compare the shape of the curves rather than the absolute values.

For the symmetric profile, the pressure difference is given by the accelerated flow, hence the pressure should be higher on the pressure side than on the suction side. This can be seen from figure 4.11a. It can also be seen that increased flow, the level of the pressure changes while the shape of the curves is fairly constant. At α_1 , which is the optimum guide vane angle, the flow hits the vane at the tip of the leading edge, i.e. pressure tap 7 or $x/c = 0$. By changing the angle of attack toward a smaller angle, the stagnation point will be shifted toward pressure tap 8 and the pressure distribution changes toward a flatter curve on the pressure side, due to an increased load on this side of

the vane. Since the distance between the vanes is decreased, the same flow rate must have a higher velocity and hence a higher acceleration from the stagnation point and the pressure difference between suction side and pressure side will increase. With the asymmetric profile, the pressure side and suction side should be opposite of the symmetric profile, according to the hypothesis presented in chapter 1. Figure 4.11c shows that this actually is the case.

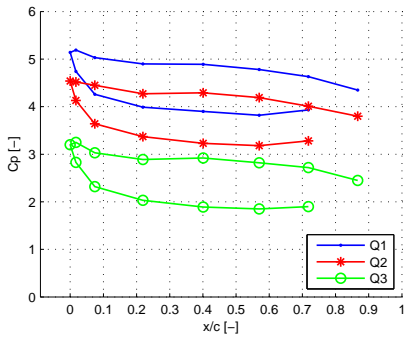
4.2.2 Wake plots

Figure 4.12 shows the results from the LDA measurements. The legends indicate the length downstream from the trailing edge of the guide vane in mm. Note that the scale is different for each plot in order to optimize the visualization of each wake. The horizontal axis is zero at the trailing edge of the guide vane and the positive side is the 'free stream side' while the negative side ends in the corresponding guide vane.

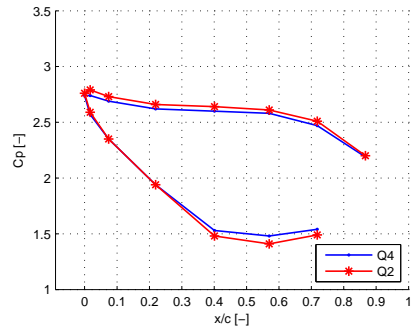
The figures show that the LDA-results seems reasonable at first glance. The velocity defect is decreasing and the width of the wake is increasing as the distance from the guide vane is increasing. By increasing the flow, and hence the free stream velocity, the velocity defect is increasing. This because of the dead water region right downstream the trailing edge. The velocity here is close to zero and with an increase of the free stream velocity, the velocity defect should also be increasing.

The results from the symmetric guide vane show that the wake is shifted slightly toward the global suction side, while with the asymmetric profile the wake is more right downstream the guide vane and it is even a tendency that it is shifted toward the global pressure side. This indicates that the change of guide vane profile actually changes the pressure distribution at the outlet of the guide vanes.

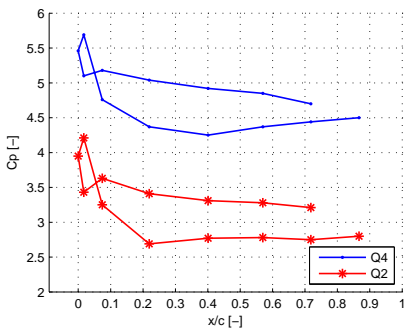
According to Bernoulli's equation the velocity should be higher on the suction side and lower on the pressure side, causing a skewness in the velocity plots. This is found in the measurements from the smaller guide vane opening, 5.0° , but for the the guide vane opening at 10.5° the tendency is rather the opposite. One explanation might be that at this opening, the pressure difference is too small to have any significant influence on the flow field. Even though the skewness is small, it changes with the change of pressure side according to the pressure measurements showed in figure 4.11 since the results from the asymmetric guide vane show a wake skewed in the opposite direction.



(a) GV1, α_1



(b) GV1, α_2



(c) GV2, α_1

Figure 4.11: Pressure coefficients

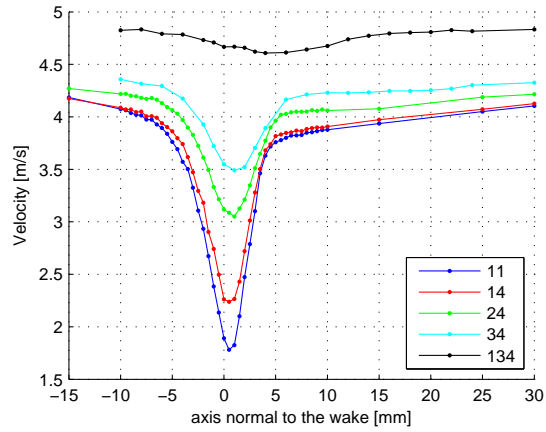
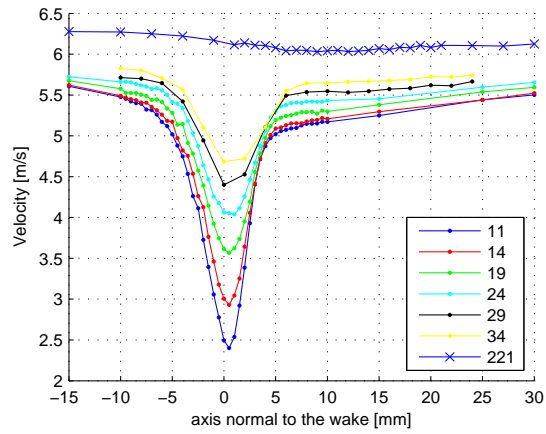
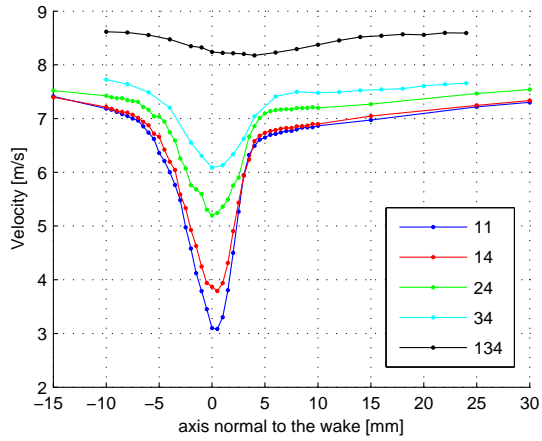
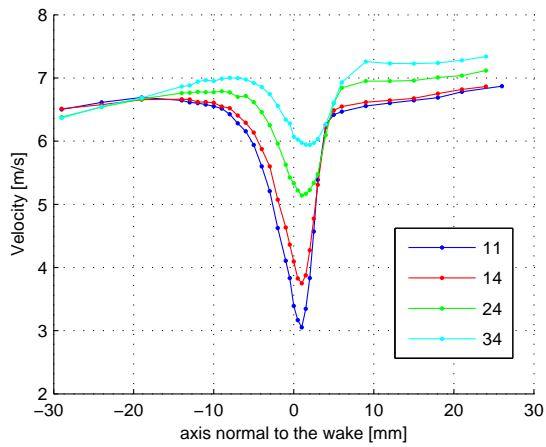
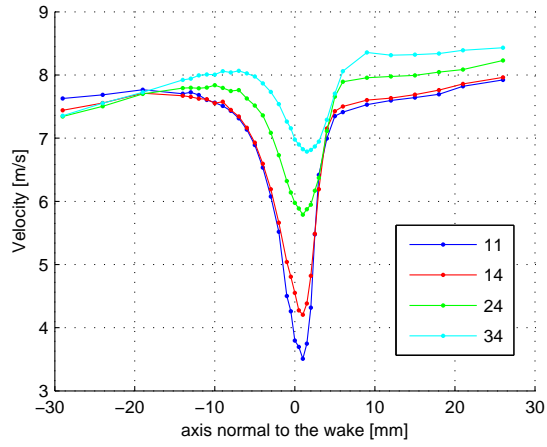
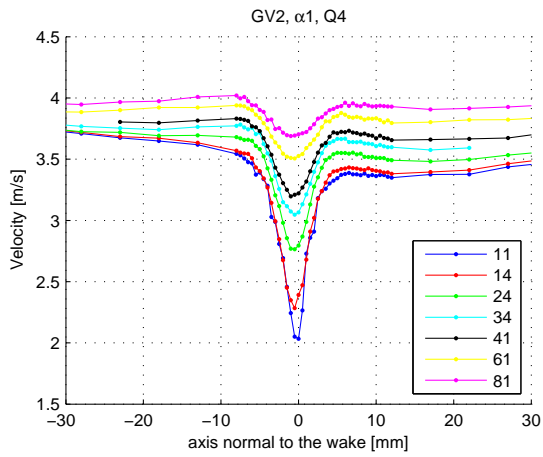
(a) GV1, Q1, α_1 (b) GV1, Q2, α_1

Figure 4.12: Wake plots

(c) GV1,Q3, α_1 (d) GV1,Q4, α_2 **Figure 4.12:** Wake plots

(e) GV1,Q2, $\alpha 2$ (f) GV2,Q4, $\alpha 1$ **Figure 4.12:** Wake plots

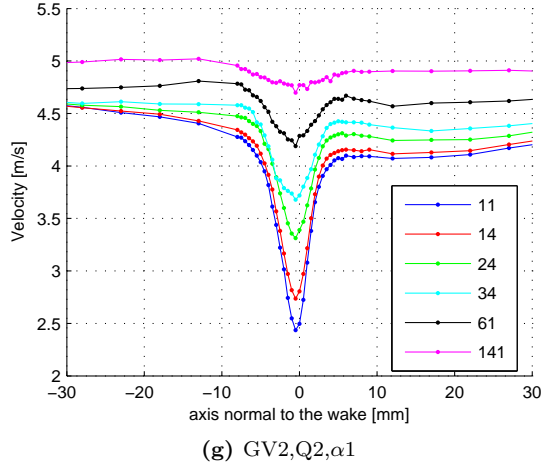


Figure 4.12: Wake plots

4.2.3 Normalized results

In wake theory, the wake is often described by a form function. This function is constant, independent of the distance downstream the trailing edge and the free stream velocity. Hence, the wake can be described by:

$$U(s, y_{\text{norm}}) = f(y_{\text{norm}}) \cdot F(U, s) \quad (4.8)$$

Where:

- U is the reference velocity
- s is the downstream distance from the trailing edge
- f is the form function
- F is a general function
- y_{norm} is a normalized axis perpendicular to the flow direction

For a 2D wake the function F and the axis y_{norm} are given by:

$$F(U, s) = \frac{U - u(s, y_{\text{norm}})}{U} \sqrt{\frac{s}{L}}, \quad y_{\text{norm}} = \frac{y}{\sqrt{sL}} \quad (4.9)$$

L is a reference distance, typically the chord length.

If F and y_{norm} are correct, the form function, f should be independent of the downstream length, s . In the guide vane cascade, the free stream velocity is an accelerated flow, hence the reference velocity, U , was set to the free stream velocity for each measurement.

It is assumed that the following function is a suitable form function for the wake:

$$u_{\text{norm}} = a + b \cdot e^{c(x-d)^2} \quad (4.10)$$

The coefficients are defined in figure 4.13 on the facing page. It should be noted that the coefficient c describes the width of the wake with a relative value. The closer to zero, the wider wake and the more negative, the narrower wake. The other coefficients describes the wake with values directly from the plot.

The velocity is normalized by the free stream velocity at each s , since it is an accelerated flow:

$$u_{\text{norm}} = \frac{u - U(s)}{U(s)} \quad (4.11)$$

Then the normalized velocity defect, b , is plotted as a function of downstream length, see figure 4.14 on the next page. As seen from the figure, the normalized values show good agreement within the different test series.

Figure 4.15 on page 54 shows the three functions $x^{-0.5}$, $1.5x^{-0.5}$ and $0.5x^{-0.5}$ for comparison with the wake-theory.

It can be seen from the figure that the self similar zone starts at about 40 mm downstream the trailing edge or $x/c \approx 0.12$. Since this method 'forces' the wake to fit a symmetric curve, this analysis will be a pure viscous analysis, not taking into account the effect of the velocity difference of the pressure side and suction side of the guide vane. However it will describe how the flow fits into traditional viscous wake theory, and if this theory is useful for this type of flow. Also, as the velocity plots have shown, this effect is rather small in this case.

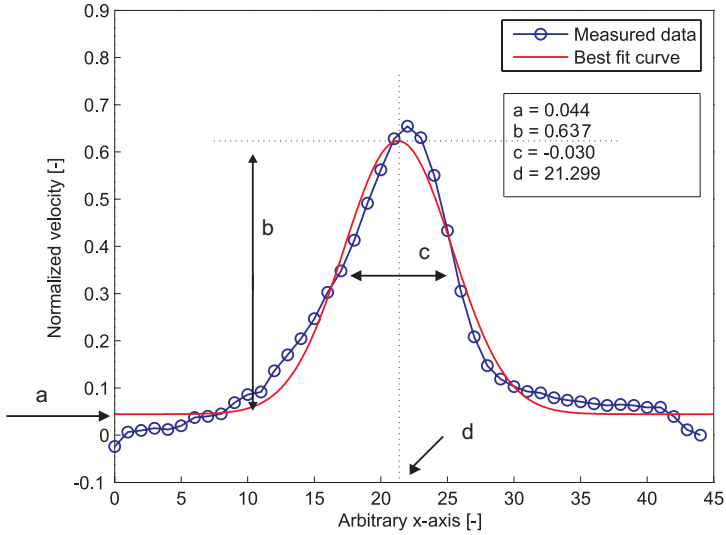


Figure 4.13: Best fit coefficient

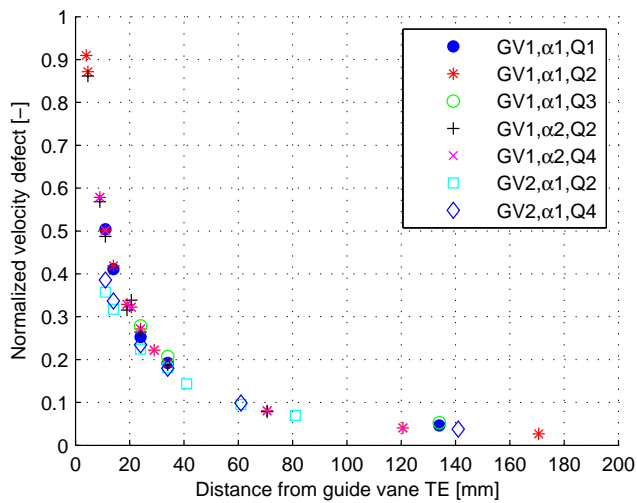


Figure 4.14: Normalized velocity defect vs. downstream distance

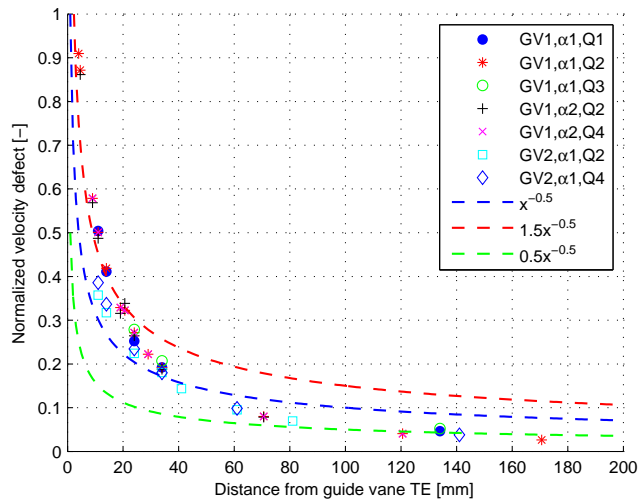
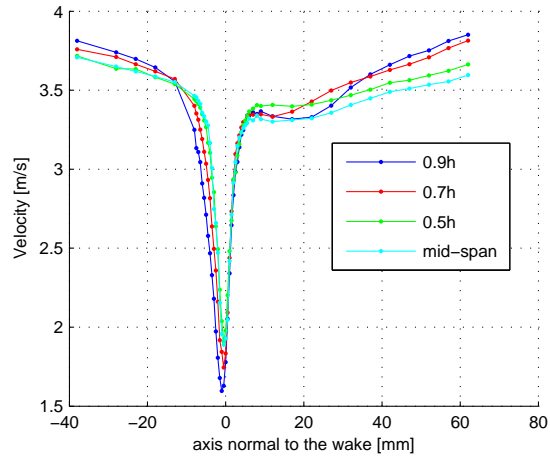


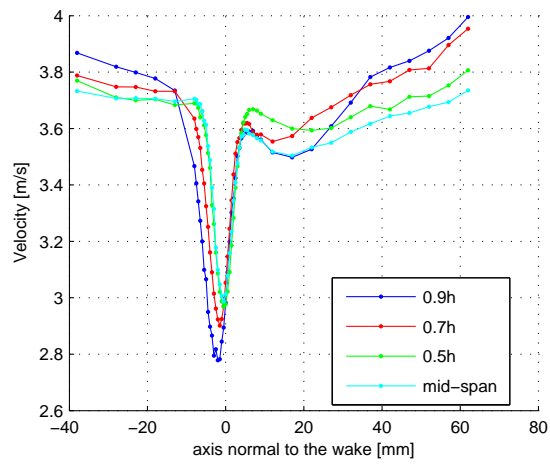
Figure 4.15: Measured data vs. wake theory

4.2.4 Wake in span-wise direction

Figure 4.16 on page 57 shows velocity plots of the velocity in constant downstream distance and varying span-wise direction. The span-wise direction is from the middle and out to the facing plate. As seen from the figures, the velocity defect is increasing and lightly more shifted toward the global pressure side. This increase in wake might be caused by the 'ears' of the guide vanes. These ears will increase the cross-section area, causing a larger wake locally. Comparing the wake at the same distance from the mid span but in opposite direction, as shown in figure 4.17 on page 57, shows quite good, but not exactly agreement. A common assumption is to assume the flow symmetric around the mid span of the guide vanes, but this results show that this may not always be true.

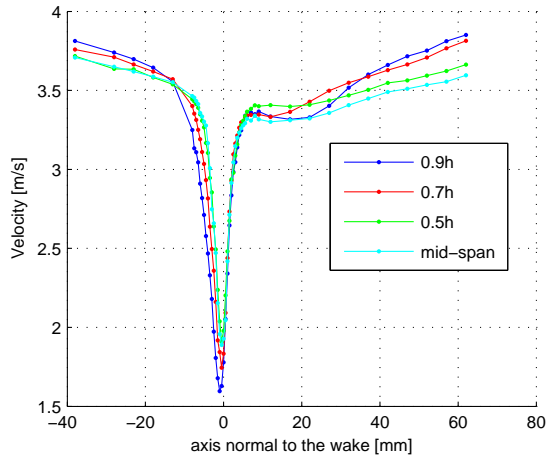


(a) Wakes 11 mm downstream TE

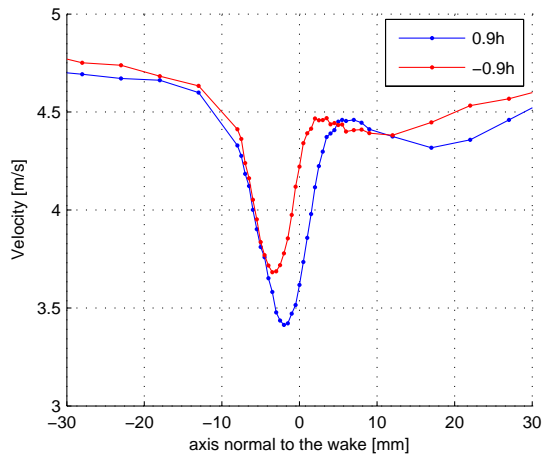


(b) Wakes 31 mm downstream TE

Figure 4.16: Wake in span wise direction



(c) Wakes 41 mm downstream TE

Figure 4.16: Wake in span wise direction**Figure 4.17:** Wake in span wise direction

4.3 Summary

During start up and shut down of the rig, the pressure was lowed so air bubbles were visible in the water. At this operation points, a vortex was observed at the inner curve, approximately at the height of guide vane 3 and 4. Unfortunately, this was outside the range of the traverse table so it could not be confirmed whether this vortex was present during the measurements or not. If the vortex was present, the velocity in the measurement section would be higher than expected from the calculated flow rate.

It was assumed that the horseshoe vortices close to the facing plates would contribute to increase the mixing in the flow and hence cause a smaller wake closer to the facing plates, but the results actually showed the opposite effect. This is probably caused by the increased area due to the ears on the guide vanes and that the horseshoe vortices not affect the flow so far from the facing plates.

In addition to the velocity defect itself, the wake will also cause a change in the direction of the relative velocity at the inlet of the runner blade. This velocity change will cause the inlet flow angle, β in figure 2.6 on page 10, to vary which will cause a varying load on the runner blade. This variation is analogous to a change in the angle of attack on a wing profile. The change in angle of attack will change the lift force on the wing, and similarly, the change in the flow angle on the runner blade will cause a varying load on the runner blade. Since this change is caused by the wake of the guide vanes, the runner blade will feel this change every time a it passes a guide vane, resulting in a varying load on the blade. This effect is dependent on the wake and the distance between the guide vane and runner. This means that the wake will be largest at full load when the guide vanes are fully open and, hence, the distance between the guide vane and runner blade are at a minimum. Kjeldesen [37] derived the change of pressure caused by change in the relative velocity for a typically high head Francis turbine and found that the pressure might vary between 1% up to 11% of the turbine's net head with the highest value for full load.

4.4 Estimated experimental uncertainty

All measurements have errors. These errors are the difference between the measured value and the true value. The total error, F , have two components: bias error, b , and random error, s . When these components are combined in a single

uncertainty number, F , the true value, V , lies within the interval:

$$V = X \pm F \quad (4.12)$$

Where X , is the sample average of the measured quantity. The individual uncertainty, F_i is defined in the standard ISO/TR 5168, [30] as:

$$F_i = \sqrt{b^2 + (t_{95} \cdot s)^2} \quad (4.13)$$

where b is the systematic uncertainty of a symmetric uncertainty interval, s the experimental standard deviation of the mean and t_{95} the 95th percentile point of the two tailed Student- t distribution. When the individual uncertainty is found, the overall uncertainty is found from:

$$F = \sqrt{\sum_{i=1}^n F_i^2} \quad (4.14)$$

In cases where the wanted parameter is calculated as a function of a measured quantity, errors in the measurements are propagated to the quantity through the function. This effect may be approximated with the Taylor series method, introducing the sensitivity coefficient, θ . Given the parameter $R = f(Y_1, Y_2, \dots, Y_n)$, θ can be calculated by:

$$\theta_i = \frac{\partial R}{\partial Y_i} \quad (4.15)$$

The dimensionless sensitivity coefficient can now be calculated as:

$$\theta_i^* = \theta_i \frac{Y_i}{R} \quad (4.16)$$

For the pitot measurements the velocity is a function of the pressure difference in the pitot tube, given by a measured height of water column in the manometer, h . Thus the velocity can be expressed by:

$$v = \sqrt{2 \cdot g \cdot h} \quad [m/s] \quad (4.17)$$

The sensitivity coefficient can now be calculated as:

$$\theta = \frac{\partial v}{\partial h} = \frac{\partial(\sqrt{2 \cdot g \cdot h})}{\partial h} = \frac{1}{2} \cdot \frac{v}{h} \quad (4.18)$$

$$\theta^* = \frac{1}{2} \frac{v}{h} \cdot \frac{h}{v} = \frac{1}{2} \quad (4.19)$$

The calculated uncertainties are:

	b	s	t_{95}	F_i
Velocity component U_x	$\pm 0.5\%$	$\pm 2.1\%$	2	$\pm 4.2\%$
Velocity component U_y	$\pm 0.5\%$	$\pm 1.7\%$	2	$\pm 3.4\%$
Kulite HKM-375 1.7 bar	$\pm 0.25\%$	$\pm 0.7\%$	2	$\pm 1.4\%$
Velocity from pitot	$\pm 0.7\%$	$\pm 0.8\%$	2	$\pm 1.3\%$

Where b is given from the manufacturer of the instruments and calibration, s from repeated measurements and t_{95} from table 7 in [30].

The position of the traverse table is assumed to have an uncertainty in the position of ± 0.1 mm based upon manufacturer's data and previous experience with the same equipment.

The pitot measurements are assumed to have an uncertainty in the reading of the pressure height of 2.0% and an additional 1.0% due to the fact that the water passing the pitot holes will contain some stagnation pressure due to the design of the pitot tube.

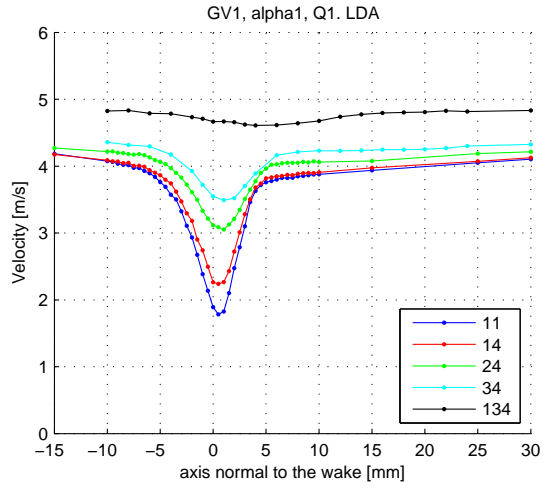
Chapter 5

Comparison of numerical and experimental results

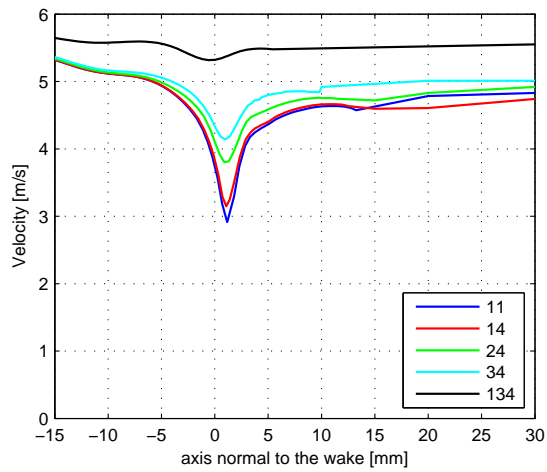
5.1 Comparison

The numerical results have been compared with the measurements by plots of velocity magnitude in the wake downstream the guide vanes. Figure 5.1 on the following page shows a comparison of velocity plots from LDA and CFD at different downstream positions. The figure shows that the wakes from the CFD-calculations have fairly the same shape as the measured one, and that the position of the wake has been very good captured. However, the CFD results show a higher free stream velocity and a narrower and less deep velocity defect. An average of all the calculations show an over-prediction of the free stream velocity of ca 15 %, an under-prediction of the depth and width of the wake of ca 25 % and 30 % respectively. The CFD-plots also show a tendency to be more skewed than the measured one.

It has not been surprising that the wakes have been under-predicted in this calculations since quite a few simplifications have been made. The CFD-model used is a 2-dimensional model, while the results from the LDA-measurements have shown that the velocity defect also will vary in the span wise direction. This means that there must be momentum transfer in this direction which again



(a) LDA results



(b) CFD results

Figure 5.1: Wake from LDA and CFD

means that the wake is 3D-dimensional. Also, the wake is highly dependent of the momentum transfer between the wall of the guide vanes and the flow and hence dependent of correct resolving of the boundary layer and correct modeling of all the viscous effects.

Some steps have been carried out in order to improve the results and also to exclude any sources of error. First the periodic boundary condition has been investigated by comparing calculations of three different geometries: A complete model of the cascade rig, including the inlet pipe and all five vanes, three stay vanes and guide vanes and only one stay vane and guide vane have been used. Due to the design of this turbine with the stay vanes close to the guide vanes it has been preferred to keep the stay vanes in order to reduce any error due to the inlet boundary condition. If the stay vanes had been removed, a non-uniform velocity field, taking into account the wake from the stay vanes should have been used. Since this is difficult to predict accurately, it has been chosen to keep the stay vanes in the numerical model.

The three different geometries, shown in figures 5.2 and 5.3 on the next page, have been meshed with the same size of the mesh cells and with a total number of ca 155000, 100000 and 30000 mesh cells respectively. The results are shown in figure 5.4 on page 65. The difference between calculating on three channels versus the whole model is negligible at the three guide vanes in the middle of the cascade. The two vanes closest to the wall will be affected by the presence of the wall and its influence on the flow. The one channel model also compares good with the other calculations, but with a little higher level on the total pressure and a little smaller pressure difference. This results have shown that simplification with the geometry gives minor influence on the results. This is in good agreement with the fact that the cascade has been designed to be symmetric in all channels.

As the LDA-measurements have shown, the wake flow is 3-dimensional. A 2D calculation will not take into account velocity variations in the span wise direction nor the effect of boundary layers on the facing plates. A calculation on a 3D model, with only one channel due to the mesh size, has been carried out in order to achieve a more realistic flow pattern. Even with only one channel, a 3D-mesh with the same cell-size as the optimum 2D-mesh will have about 500000 mesh cells, dependent of the resolution in span wise direction. The results are shown in figure 5.6 and 5.7 on page 67. In figure 5.6 the velocity defect in different span wise positions at a distance 11 mm downstream the trailing edge are compared with LDA results at the same downstream distance. The figure

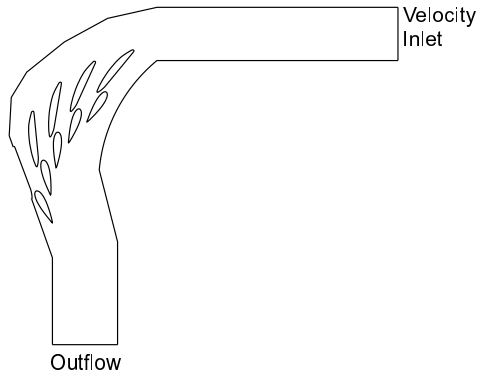


Figure 5.2: Complete geometry

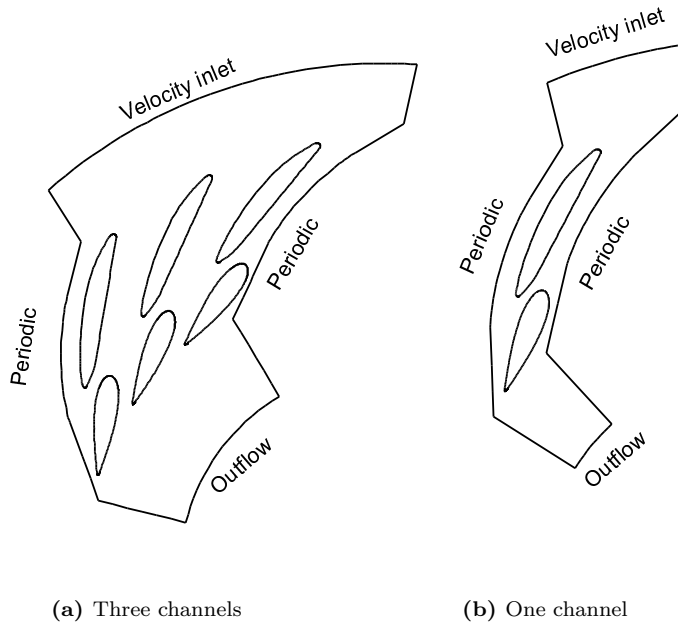


Figure 5.3: Simplified geometry

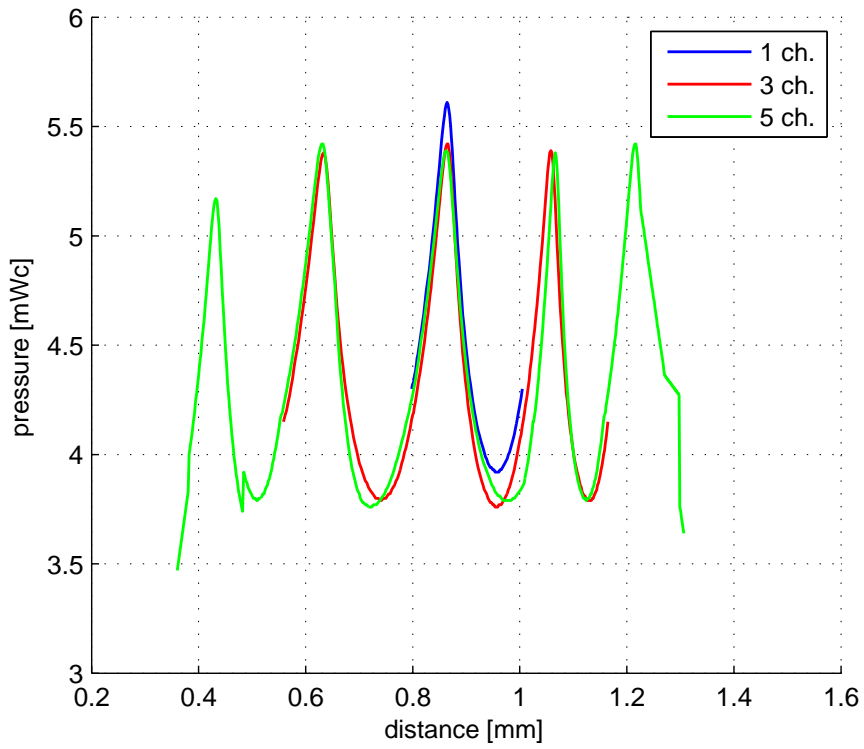


Figure 5.4: Pressure plot from different simplifications

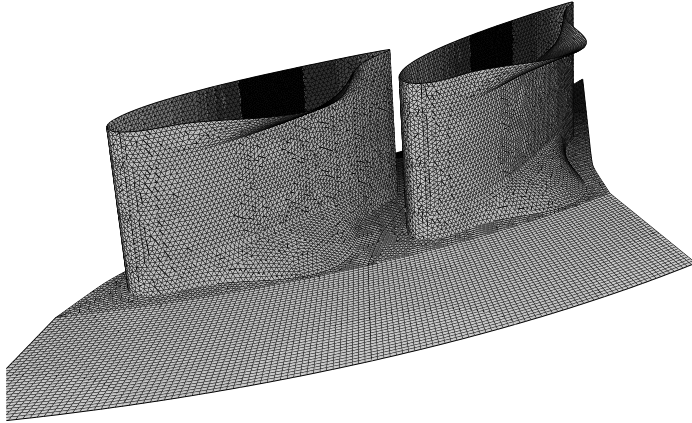


Figure 5.5: 3D Mesh around the guide vane

shows that the CFD still under-predicts the depth of the wake, but the width and free stream velocity have been better captured. An average of all the 3D-calculations gives an over-prediction of the free stream velocity of ca 5 % and an under-prediction of the depth and width of ca 15 % and 5 % respectively. Figure 5.7 shows that the CFD-calculations are much more symmetric around the mid span than the LDA-measurements. This indicates that there have been some factors in the cascade rig causing the flow to be non-uniform that not have been captured in the CFD calculations.

A difference between the experimental and numerical results has not been unexpected, since the experiment contained some factors that is hard to capture by CFD. It has been experienced quite a lot of small leakages on the model rig, which probably caused additional secondary flow and contributed to make the flow field non-uniform. Also the horse-shoe vortices at the facing plates will affect the flow, but none of these effects will be captured in a CFD-model. It has also been observed a vortex at the inner curve of the cascade model, approximately at the height of guide vane 4. This vortex has been visible due to the low pressure with resolved air bubbles during start up and shut down of the rig. The location of the vortex has been outside the traversing range of the LDA so it could not be confirmed whether it was present during the measurements or not. Assuming the presence of a vortex, the main flow in the rest of the

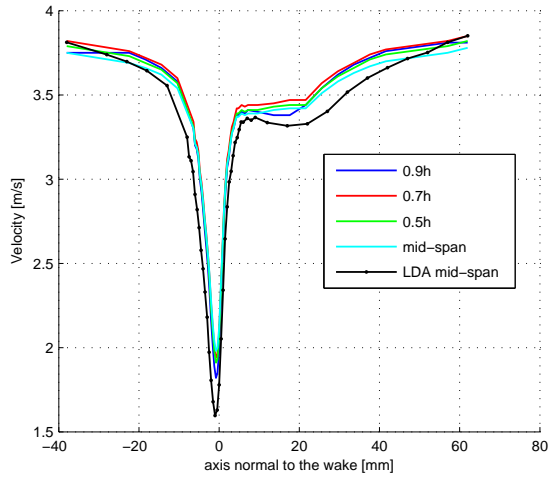


Figure 5.6: Wakes from 3D CFD

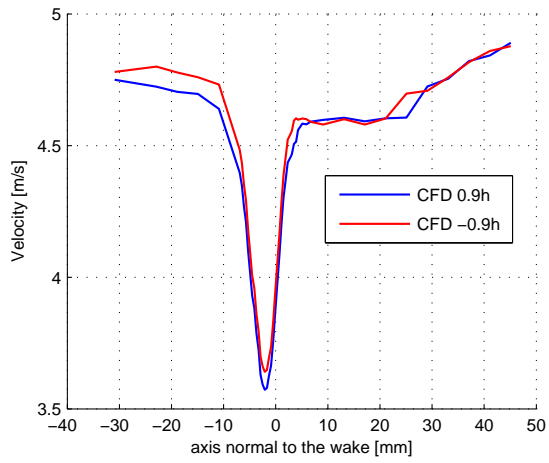


Figure 5.7: Span wise wake from 3D CFD

flow field will get a higher velocity due to the dead water region caused by the vortex. A higher main flow will result in a larger wake and might be a cause of error in this case.

Even though the 3D-model has given the best agreement with the measurements, the large mesh size makes this model poor fitted, from a time perspective point of view, for doing several calculations to compare different guide vane profiles. Since it strictly speaking has been the relative difference of the effect of using different guide vane profiles that has been the main focus, an extra effort has been done in analyzing the 2D-data. The wake plots have been normalized according to the same method as the LDA-measurements and plotted in the same figure, see figure 5.8 The figure shows how the normalized CFD-results

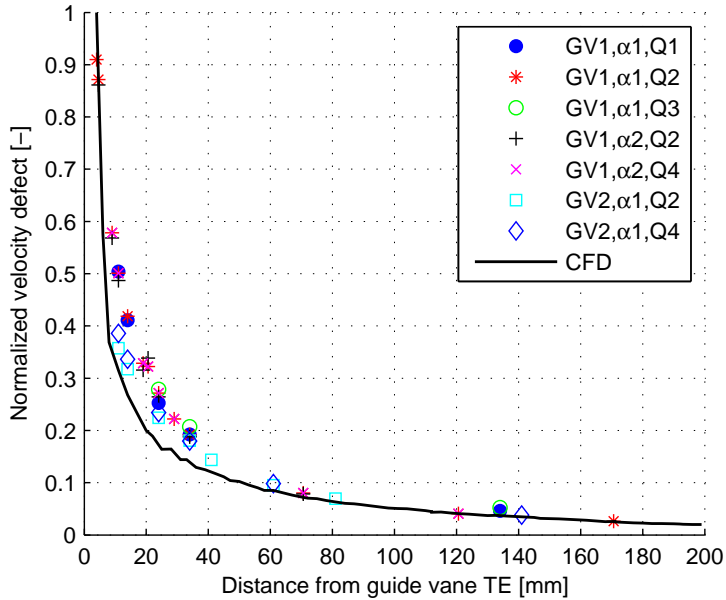


Figure 5.8: Normalized CFD results

agrees fairly well with the normalized measured data. This fact together with the fact that the pressure distribution did not change much with the different calculations as the velocity defect, should support the theory that the CFD-calculations will at least capture relative changes in the model. Hence, the

results from the preliminary calculations have been considered trustworthy.

5.2 Additional CFD-calculations

In order to verify that different pressure distribution gives different load on the runner, a simplified 2D model of rotor/stator interaction has been carried out. Since the purpose has been to see the relative changes on the dynamic load on the runner blade, it has been assumed that a 2D model would be sufficient. It has rather been emphasized to carry out more simulations than few absolutely correct ones. A complete 3D unsteady guide vane / runner simulation is very time consuming and due to the time limit of this work a simplified model has been chosen.

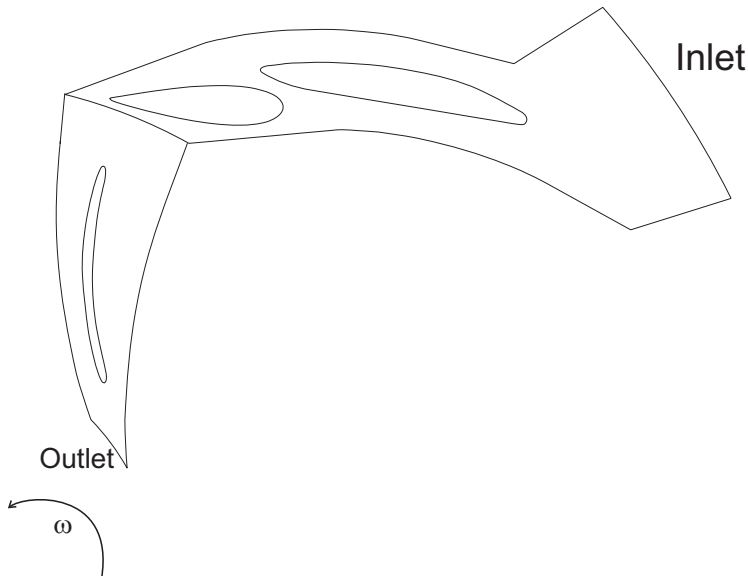


Figure 5.9: Simplified geometry

The geometry in the model has been one stay vane, one guide vane and one runner blade. The calculation method used has been the *sliding mesh* approach

in Fluent. This approach is the most accurate model since it performs a fully unsteady calculation. The time step size has been set so the two meshes does not rotate more than one mesh cell relative to each other per time step since larger rotational speed may cause divergence in the calculations [23].

The rotational speed of the runner has been adjusted in order to fit the flow from the guide vanes and in order to give a flow through the runner blade channel without back-flow or separation. A simplified, 2D runner blade has been rotated

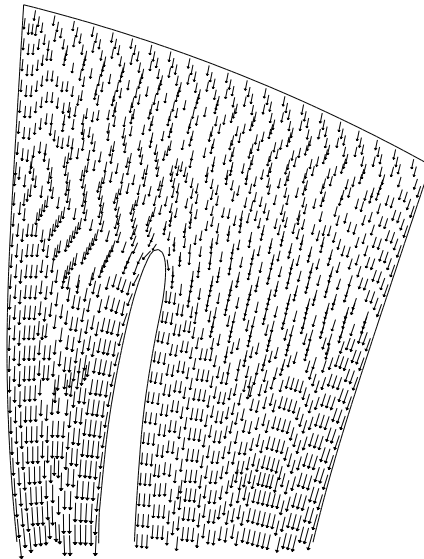


Figure 5.10: Velocity vectors at the inlet of the runner blade

downstream guide vanes with different profiling, and the torque on the runner blade has been used as comparison for the dynamic load. The calculations have been supposed converged when a steady oscillation of the torque has been achieved. After a converged solution has been achieved, the calculations have been run for some time, gathering time dependent data. A typically plot of the time varying load for the symmetric profile is shown in figure 5.11 on the next page.

A comparison of the runner blade torque for the different profiles is given in table 5.1 on page 73 and shown in figure 5.12 on page 72. The table also shows

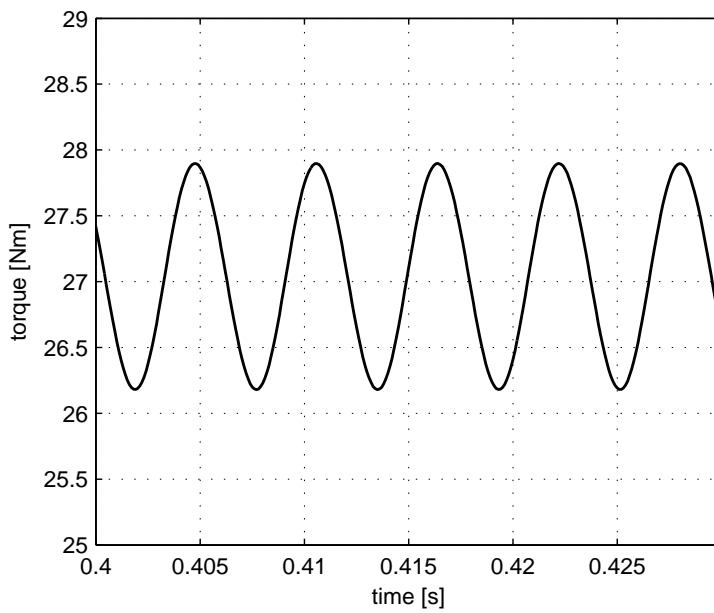


Figure 5.11: Torque vs. time

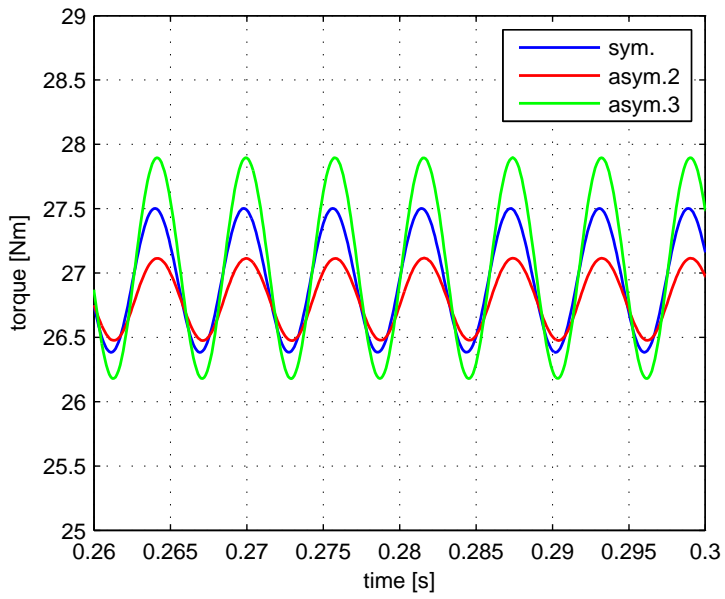


Figure 5.12: Torque on runner blade

the losses in the flow through the guide vanes. The losses have been calculated as the difference between the total pressure at the inlet and outlet and normalized with the net head of the turbine. Finally, the torque on the guide vane around the guide vane center bolt have been calculated in order to see how the guide vane profiling will influence on this. The results have been summarized in table 5.1.

Guide vane	Runner torque (ΔM [Nm])	Relative torque ($\Delta M/\Delta M_{\text{sym}}$ [-])	Relative losses ($\Delta H/\Delta H_{\text{sym}}$ [-])
Symmetric	0.56	100	100
Asymmetric 2	0.33	58	92
Asymmetric 3	0.86	153	106

Table 5.1: Results for different guide vane profiling

The results clearly shows that profiling of the guide vanes will influence on the runner torque. The trend is as posted in the hypothesis, that more uniform pressure distribution will give less load variation on the runner blade. In this case the difference is rather small, but the trend is clear. The small difference might be due to the fact that this is a well designed turbine and the level of pressure pulses is generally low. Also, the flow is quite low in order to compare with the LDA-measurements and, hence, limited of the flow in the cascade rig.

The losses for the correct asymmetric profile are smaller than for the symmetric one. This is probably due to the fact that this profile is slightly slimmer than the symmetric one and also fits the flow angle very well. The higher loss for the wrong asymmetric profile might be caused by the fact that this profile have the poorest fit to the flow angle, forcing the flow in an unfavorable direction and guiding the flow a bit away from the main flow direction. If a guide vane with this kind of profiling is used in a turbine, this will of course be taken into consideration when designing the guide vanes so the losses not necessary have to be higher. However, the results shows that the profiling have negligible influence on the losses in the flow when the guide vanes are designed to fit the flow angle. This means that the guide vanes can be designed in order to reduce the load variation on the runner without increasing the losses in the flow.

5.3 Summary

After the numerical and experimental results have been compared, it can be concluded that the CFD gives acceptable results. Even if the absolute correct values have not been achieved, the normalized results have shown that the physics of the flow has been well captured. Hence, it should be reasonable to assume that relative changes in the geometry would be captured in a good way with CFD.

It is no doubt that correct profiling of the guide vanes can influence on the pressure distribution and that a more uniform pressure distribution reduces the dynamic load on the runner. This can be achieved without increasing the losses in the flow.

There has not been carried out any calculations regarding the efficiency of the turbine, but it is assumed that as long as the flow from the guide vanes still gives optimal inlet conditions on the runner, the efficiency should not have to be sacrificed to achieve reduced load on the runner blades.

Chapter 6

Conclusions and further work

6.1 Conclusions

An experimental and numerical study of the unsteady flow at the inlet of the runner of a Francis turbine has been carried out. The main goal has been to investigate how the profiling of the wicket gate can contribute to reduce the dynamic load on the runner blades by creating a more uniform pressure distribution at the inlet of the runner.

LDA measurements in a cascade rig have shown that the viscous wake behind the guide vanes can be described by classic wake theory, even though it is a tendency that the wakes mixes out somewhat faster, due to the accelerated flow field.

The CFD calculations have shown a tendency to under-estimate the wake and over-estimate the free stream velocity. This might be because of CFD's lack of resolving all the momentum transfers between the guide vanes and the water. In this case there have also been some uncertainties in the measurements due to leakage flow over the guide vane and extra leakage in the cascade rig which have caused secondary flow which not has been captured by the CFD. The 2D-calculations have shown a deviation from the measurements with ca 25 %, while

the 3D-calculations have a deviation of ca 15 %, which has been assumed to be acceptable. This has shown that the wake flow is 3-dimensional with momentum transfer in all directions. Still, 2D-calculations have given good agreement with the relative, normalized results. This has indicated that even simplified 2D-calculations will be suitable to capture relative changes, even though the absolute values might differ from the measurements.

Pressure measurements around the the mid-span of a guide vane have shown that the pressure distribution has been according to the expected results. With a symmetric profile, the pressure is highest at the stagnation point and the guide vane will have a pressure distribution given by the flow field with a certain pressure side and suction side at the trailing edge. By changing the angle of attack, the stagnation point will move according to the new flow angle. By profiling the guide vane asymmetric, the pressure side and suction side on the guide vane is either shifted or amplified. CFD-calculations have shown that with the local pressure and suction side on the guide vane opposite to the one caused by the accelerated flow, the pressure will counteract and cause a more uniform overall pressure distribution. Unsteady CFD-calculations of a simplified wicket gate / runner interaction have shown that a more uniform pressure distribution will give less torque variation on the runner blade. Hence the profiling of the guide vanes might be designed in order to reduce the dynamic load on the runner blades. This profiling have not increased the loss in the flow past the guide vanes which means that reducing the dynamic load on the runner should not reduce the efficiency of the turbine.

It should also be mentioned that even though this profiling tends to reduce the dynamic load on the runner, turbines might very well operate smoothly even with the 'wrong' profiling on the wicket gate. Together with the parameters discussed in this thesis, the distance between the wicket gate and the runner, the flow rate, the thickness of the blades and the blade leaning are some other important design parameters that will influence on the overall dynamic load.

6.2 Further work

As mentioned, the inlet flow in a Francis turbine is highly complex and there are still further topics to research in the future. As for the viscous wake, some work has been carried out in order to reduce the viscous wake by use of vortex generators. Work presented by Arndt et al. [5] discusses the effect on the wake

by using vortex generators. If this is further investigated it might be introduced in turbines in order to reduce the effects of the wake flow.

Further and more comprehensive measurements of the wake flow will also increase the understanding of this complex flow pattern. 3D LDA measurements will give a more complete picture of the flow that obviously is 3-dimensional. PIV (Particle image velocimetry) measurements should be used in order to capture the dynamic effects in the wake flow. It is well known that the wake consists of dynamic effects and by using PIV this could also be taken into the analysis of the wake flow.

A combined measurement series with strain gauges on the runner blades and pressure pulses at the inlet of the runner would give more information of the connection between the influence of the pressure pulses in the area between the wicket gate and runner and the real load on the runner blades. With such a measurement set up, the efficiency of the turbine could also be measured with different profiles on the wicket gate in order to give a more complete understanding of this complex phenomenon.

Bibliography

- [1] Ø. Antonsen. Ustabile driftsområder for Francisturbiner. Masters thesis, Norwegian University of Science and Technology, 2003. In Norwegian.
- [2] Ø. Antonsen and T. K. Nielsen. CFD simulations of von Karman vortex shedding. In *22nd IAHR Symposium*, Stockholm, 2004.
- [3] Ø. Antonsen, T. K. Nielsen, and O. G. Dahlhaug. Experimental and theoretical investigations of the flow field at the inlet of a francis runner. In *Hydro Vision. Portland, Oregon*, 2006.
- [4] Ø. Antonsen, T. K. Nielsen, O. G. Dahlhaug, and J. T. Billdal. Pressure pulses in francis turbines vs. guide vane design. In *23th IAHR Symposium - Yokohama*, 2006.
- [5] R. Arndt, M. Kjeldsen, and M. Wosnik. Dynamics and control of hydrofoil wakes. In *59th Annual Meeting of the APS Division of Fluid Dynamics*, 2006.
- [6] R. E. A. Arndt, M. Kjeldsen, C. C. S. Song, and A. Keller. Analysis of cavitating wake flows. In *Proceedings of the Hydraulic Machinery and Systems 21th IAHR Symposium. Lausanne*, 2002.
- [7] J. T. Billdal, H. I. Anderson, H. Brekke, and B. Holt. A study of nonstationary flow effects on a Francis turbine runner caused by the guide vane effects. In *XVII IAHR symposium. Beijing, China*, 1994.
- [8] J. T. Billdal and B. G. Holt. Three Gorges project: Review of GE Energy Norway's hydraulic design. In *20th Int. IAHR Symposium on Hydraulic Machinery and Systems.*, 2000.

-
- [9] B. Boulet. *Fundamentals of signals & systems*. Da vinci engineering press, 2006.
- [10] H. Brekke. A review in oscillatory problems in Francis turbine and simulation of unsteady flow in conduit systems. In *XVII IAHR Symposium. Beijing, China*, 1994.
- [11] H. Brekke. *Grunnkurs i hydrauliske strømningsmaskiner. Lecture notes in Norwegian*. NTNU, Trondheim Norway, 1998.
- [12] H. Brekke. Hydraulic turbines. design, erection and operation. Norwegian University of Science and Technology, 2001.
- [13] C. E. Brennen. *Hydrodynamics of Pumps*. Oxford Science Publications, 1994.
- [14] X. Chen. *Theoretical and experimental study of flow through the double cascade of a Francis turbine*. PhD thesis, Norwegian Institute of Technology, 1992.
- [15] X. Chen, C. C. S. Song, K. Tani, Shinmei, K. Niikura, and J. Sato. Simulation of pressure fluctuations in pump-turbines induced by runner-guide vane interactions. In *20:th IAHR Symposium*, Charlotte, North Carolina, aug 2000.
- [16] G. D. Ciocan and J. L. Kueny. Experimental analysis of rotor-stator interaction in a pump turbine. In *23th IAHR Symposium, Yokohama*, 2006.
- [17] Dantec Dynamics Homepage. LDV measurements principles. <http://www.dantecdynamics.com/LDA/Princip/Index.html>. [Accessed 22 December 2005].
- [18] R. M. Donaldson. Hydraulic-turbine runner vibrations. In *Transaction of the american society of mechanical engineers*, volume 79, pages 1141–1147. ASME, 1957.
- [19] L. E. Drain. *The Laser Doppler Technique*. John Wiley & Sons, 1986.
- [20] D. M. Driver and G. G. Mateer. Wake flow in adverse pressure gradient. *International Journal of Heat and Fluid flow*, 23:564–571, 2002.
- [21] F. Durst, A. Melling, and J. H. Whitelaw. *Principles and practice of laser-doppler anemometry*. Academic press, 1981.

-
- [22] S. Eide. *Numerical analysis of the head covers deflection and the leakage flow in the guide vanes of high head Francis turbines*. PhD thesis, Norwegian University of Science and Technology, 2004.
- [23] Fluent Inc. *Fluent user's guide*, 2005.
- [24] GE Energy. Rotor-stator analysis (rsi)(wg & runner). 2006. Internal calculations, 2006.
- [25] R. J. Goldstein. *Fluid Mechanics Measurements*. Taylor & Francis, 1996.
- [26] C. A. Gongwer. A study of vanes singing in water. In *Transaction of the american society of mechanical engineers*, volume 74, pages 432–438. ASME, 1952.
- [27] G. Heskestad and D. R. Olberts. Influence of trailing edge geometry on hydraulic-turbine-blade vibration resulting from vortex excitation. In *Journal of Engineering for Power*, pages 103–110. ASME, apr 1960.
- [28] S. Huang. A numerical study on the impeller-diffuser interaction of a multi-stage centrifugal pump. In *21th IAHR Symposium. Yokohama*, 2006.
- [29] International Electrotechnical Commission. *IEC 60193. Hydraulic turbines, storage pumps and pump-turbines - Model acceptance tests*. International Electrotechnical Commission, 1999.
- [30] International Organization for Standardization. *ISO/TR 5168, 1978: Measurement of fluid flow - Estimation of uncertainty of a flow-rate measurement*. International Organization for Standardization, 1978.
- [31] J. Jernsletten. Experimental analysis of pressure pulsations in a reversible pump turbine. In *17th IAHR Symposium*, 1994.
- [32] J. Jernsletten. *Analysis of non-stationary flow in a Francis reversible pump turbine runner*. PhD thesis, Norwegian Institute of Technology, 1995.
- [33] D. Jošt and L. Škerget. Separate and coupled CFD simulation of a flow in a Francis turbine. In *20:th IAHR Symposium*, Charlotte, North Carolina, aug 2000.
- [34] T. Kaechele, C. Hauff, and T. Aschenbrenner. Discussion of several numerical approaches for the stator-rotor interactions. In *20:th IAHR Symposium*, Charlotte, North Carolina, aug 2000.

-
- [35] M. Keller, P. Dörfler, M. Sallaberger, and M. Sick. Rotor-stator interaction in pump turbines - numerical prediction and experiment. In *Hydro 2005*, 2005.
- [36] M. Kjeldsen. *Cavitation in hydraulic machinery*. PhD thesis, Norwegian Institute of Technology, 1996.
- [37] M. Kjeldsen. Analytical analysis of runner wake passage. FDB report no. 226, 2006.
- [38] M. Kjeldsen, R. E. A. Arndt, and M. Effertz. Spectral characteristics of sheet/cloud cavitation. *Journal of Fluid Engineering*, September 2000, Vol 122., 122:481–487, 2000.
- [39] T. Kubota, F. Han, T. Kuwayama, and J. Masuda. Effect of grid size in CFD code on flow through Francis turbine. In *20:th IAHR Symposium*, Charlotte, North Carolina, aug 2000.
- [40] C. Larsson. *Experimental and theoretical analysis of inlet flow of a Francis Turbine Runner*. PhD thesis, Norwegian University of Science and Technology, 2003.
- [41] C. Larsson. Experimental investigation of the transient inlet flow of a Francis turbine runner. In *22nd IAHR Symposium*, 2004.
- [42] P. Li. *An Experimental Investigation of Velocity Distribution and Head Loss of Oscillatory Flow in a Rectangular Duct with Sand Roughness*. PhD thesis, Norwegian University of Science and Technology, 2004.
- [43] A. Lipej, D. Jost, P. Meznar, and V. Djelic. Numerical analysis of rotor-stator interaction in a reversible pump-turbine - pump mode. In *23th IAHR Symposium - Yokohama*, 2006.
- [44] P.-Y. Lowys, J.-L. Deniau, E. Gaudin, P. Leroy, and M. Djatout. On-board runner dynamic measurements. In *Hydrvision. Portland, Oregon*, 2006.
- [45] P.-Y. Lowys, J.-L. Deniau, E. Gaudin, P. Leroy, and M. Djatout. On-board runner dynamic measurements. In *HydroVision*, 2006.
- [46] E. Lund. *Hydrauliske trykksvingninger i omdreiningshulrommet mellom ledeapparat og løpehjul i en Francisturbin*. PhD thesis, Norwegian Institute of Technology, 1966. In Norwegian.
- [47] MathWorks Inc. *Matlab R14 Documentation*, 2005.

-
- [48] B. Nennemann, T. Vu, and M. Farhat. CFD prediction of unsteady wicket gate-runner interaction in Francis turbines: A new standard hydraulic design procedure. In *Hydro 2005*, 2005.
- [49] D. Newland. *An introduction to random vibrations, spectral & wavelet analysis*. Longman Scientific & Technical, 1993.
- [50] C. Nicolet, N. Ruhonnet, and F. Avellan. Onedimensional modeling of rotor stator interaction in francis pumpturbine. In *23th IAHR symposium - Yokohama*, 2006.
- [51] T. K. Nielsen. *Dynamisk dimensjonering av vannkraftverk*. NTNU, 1990. In Norwegian.
- [52] T. K. Nielsen and Ø. Antonsen. CFD simulations of von Karman vortex shedding. In *11th International meeting of the work group on the behavior of hydraulic machinery under steady oscillatory conditions*, Stuttgart, oct 2003.
- [53] M. Oledal. *Cacitation in Complex Separated Flows*. PhD thesis, Norwegian University of Science and Technology, 2001.
- [54] M. Page, É. Thérooux, and J.-Y. Trépanier. Unsteady rotor-stator analysis of a Francis turbine. In *22nd IAHR Symposium*, 2004.
- [55] J. G. Proakis and D. G. Manolakis. *Digital signal processing*. Prentice-Hall International, INC, 1996.
- [56] R. Quian, C. Deschênes, R. Fraser, and Y. Maciel. Flow field measurements around a guide vane with partikle image velocimetry. In *Hydrovision, Portland, Oregon*, 2006.
- [57] R. Quian, C. Deschenes, R. Fraser, and Y. Maciel. Flow fld measurements around a guide vane with particle image velocimetry. In *Hydrovision, Portland, Oregon*, 2006.
- [58] A. Ruprecht. Unsteady flow analysis in hydraulic turbomachinery. In *20:th IAHR Symposium*, Charlotte, North Carolina, aug 2000.
- [59] A. Ruprecht, M. Heitele, T. Helmrich, W. Moser, and T. Aschenbrenner. Numerical simulation of a complete Francis turbine including unsteady rotor/stator interactions. In *20:th IAHR Symposium*, Charlotte, North Carolina, aug 2000.

-
- [60] C. Segoufin, F. Mazzouji, P.-Y. Lowys, and J.-L. Deniau. Numerical investigation of unsteadiness in hydraulic turbines. In *Hydrovision. Portland, Oregon*, 2006.
- [61] C. Segoufin, F. Mazzouji, P.-Y. Lowys, and J.-L. Deniau. Numerical investigation of unsteadiness in hydraulic turbines. In *Hydrovision, Portland, Oregon*, 2006.
- [62] C. Segoufin, F. Mazzouji, P.-Y. Lowys, and J.-L. Deniau. Numerical investigation of unsteadiness in hydraulic turbines. In *23th IAHR Symposium - Yokohama*, 2006.
- [63] H. E. Stepanik. *Reversible Francis Pump-Turbines: Improvement of part load performance by changes on the design of impeller blades*. PhD thesis, Norwegian Institute of Technology, 1991.
- [64] A. J. Stepanoff. *Centrifugal and axial flow pumps : theory, design, and application*. New York , Wiley, 1957.
- [65] H. Tennekes and J. L. Lumley. *A first course in turbulence*. MIT Press, 1987.
- [66] TSI inc. *TSI manual*, 1990.
- [67] M. P. Tulin. The separation of viscous drag and wave drag by means of the wake survey. Technical report, Navy Department, The David W. Taylor Model Basin. Washington 7. D.C, 1951.
- [68] T. Vekve. *An experimental investigation of draft tube flow*. PhD thesis, Norwegian University of Science and Technology, 2004.
- [69] R. Vennatrø. *An experimental and theoretical analysis of non-steady turbulent flow in circular smooth pipes*. PhD thesis, Norwegian University of Science and Technology, 2000.
- [70] T. C. Vu and B. Nennemann. Modern trendt of CFD application for hydraulic design procedure. In *23th IAHR Symposium - Yokohama*, 2006.
- [71] R. E. Walpole, R. H. Myers, and S. L. Myers. *Probability and statistics for engineers and scientists*. Prentice Hall International, INC, sixth edition, 1998.
- [72] H. Wang and H. Tsukamoto. Numerical analysis of pressure fluctation due to rotor-stator interaction in a diffuser pump by vortex method. In *20:th IAHR Symposium*, Charlotte, North Carolina, aug 2000.

-
- [73] F. M. White. *Viscous fluid flow*. McGRAW-Hill, second edition, 1991.
- [74] F. M. White. *Fluid Mechanics*. McGRAW-Hill, fourth edition, 1999.
- [75] XFOIL software. <http://web.mit.edu/drela/Public/web/xfoil/>. [Accessed 12 October 2004].
- [76] S. Q. Yang. Boundary shear stress, velocity distribution and wall functions in smooth 3-d channels. In *20:th IAHR Symposium*, Charlotte, North Carolina, aug 2000.
- [77] M. V. Zagarola and A. J. Smits. Scaling of the mean velocity profile for turbulent pipe flow. *Phys. Rev. Lett.*, 78(2):239–242, Jan 1997.
- [78] R. K. Zeytounian. *Theory and Applications of Viscous Fluid Flow*. Springer, 2004.
- [79] A. Zobeiri, J.-L. Kuenny, M. Farhat, and F. Avellan. Pump-turbine rotor-stator interaction in generating mode: Pressure fluctuation in distributor channel. In *23th IAHR Symposium - Yokohama*, 2006.

Appendices

Appendix A

Papers

Papers submitted and presented at various conferences as a part of the work with this thesis will be presented in the following sections.

A.1 IAHR Stockholm, Sweden. 2004

CFD simulation of von Karman vortex shedding

Author	Firm / Institution	City, Country	Lecturer (x)
<i>PhD student Øyvind Antonsen</i>	<i>Norwegian University of Science and Technology</i>	<i>Trondheim, Norway</i>	<i>x</i>
<i>Professor Torbjørn K Nielsen</i>	<i>Norwegian University of Science and Technology</i>	<i>Trondheim, Norway</i>	

Abstract

Empirical formula for estimating the frequency of the trailing edge vortex shedding is based on Strouhal's number and numerous experiments published in several papers during 1950 – 60. These experiments have resulted in formulas which is still in frequently use for detailing the trailing edge geometry on trailing edges of stay vanes, guide vanes and runner vanes.

In his Master thesis, Øyvind Antonsen carried out 2- and 3- dimensional CFD simulations of plates with different edge geometry. The paper gives a resume of the simulations done in this master study and compares the results with the previous experiments.

The goal has been to determine whether analysis based on CFD is sufficient for predicting frequency and amplitudes of these vortices. By comparing with the results published in previous experiments, it seems like the frequency is well represented even by 2D simulations. Considering the time aspect in substantial more intensive computer work for 3D simulations, this is an interesting result itself.

Most experiments are carried out on flat plates with profiled edges. The simulations have been carried out both on flat plates but also on actual stay vane geometries giving slightly different results.

The calculated frequencies are very much in accordance with the empirical formula suggested by Heskestad et al. with some minor adjustment.

Concerning the amplitudes the simulations is more difficult to interpret. It had been desirable to find a similar empirical formula for the amplitude as for the frequency. As far as we know, few authors have handled the amplitude as such. The common practice when designing the trailing edge is to assume that high frequency gives low amplitudes. This implies an assumption of constant energy in the fluctuation independent on the frequency.

By using dimensional analysis, the paper presents a suggestion of an experimental investigation to give more light to the problem.

Résumé

La formule empirique pour estimer la fréquence de la perte de vortex de rebord arrière est basée sur le nombre de Strouhals et sur de nombreuses expériences édités en plusieurs journal pendant 1950 - 60. Ces expériences ont eu comme conséquence les formules qui est toujours dedans fréquemment utilisation pour détailler la géométrie de rebord arrière sur les rebords arrière des aubes fixes, des aubes direchaices des la roue aubes.

Le but a été de déterminer si l'analyse basée sur le CFD est suffisante pour la fréquence et les amplitudes de prévision de ces vortex. En rivalisant avec les résultats édités dans des expériences précédentes, il semble comme la fréquence est bien représentée même par les 2D simulations.

En ce qui concerne les amplitudes il est plus difficile interpréter les simulations. Il avait été souhaitable de trouver une formule empirique semblable au l'amplitude et à la fréquence. Peu d'auteurs ont manipulé l'amplitude en tant que telle. La pratique courante quand concevoir le rebord arrière doit supposer que la haute fréquence donne de basses amplitudes. Ceci implique une acceptation d'énergie constante dans la fluctuation indépendante sur la fréquence.

Introduction

The occurrence of von Karman vortex train from the outlet edge is a well-known phenomenon and very important to take into consideration when dealing with hydraulic design in general. The classic theory is developed for flow around a cylinder. For hydro turbines, the frequency of the vortex train is possible to determine by empirical formulas with sufficient accuracy.

The pressure amplitude is even more important, but is not that easy to determine. This paper reports CFD calculations of vortex train, which was done during a Master study. The frequencies at various geometries and flow conditions was calculated and fitted very well to the empirical formulas. During this work, we have discussed various approaches to determine the amplitude as well. Dimensional analysis is a good way of enlighten the phenomenon. At this stage, some ideas are presented, and the mentioned CFD calculations indicate that the result of the dimensional analyses might be worthwhile to follow up with experiments.

Theoretical approach

Using dimensional analysis is often an illustrating way of approaching physical phenomena. For flow around a cylindrical object, identifying the properties that the frequency, f , probably is a function of gives:

$$f = f(D, \rho, \mu, U) \quad (1)$$

D – diameter [m]

ρ – density [kg/m^3]

μ – dynamic viscosity [$\text{kg}/(\text{ms})$]

U – free stream velocity [m/s]

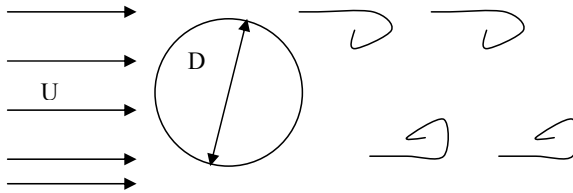


Figure 1 Flow around a cylinder

According to Buckingham's π theorem, 5 variables and 3 dimensions gives 2 π numbers. On dimensionless form, the equation reduces to:

$$\pi_1 = F(\pi_2) \quad (2)$$

The two π numbers are:

$$\pi_1 = \frac{fD}{U} \text{ Strouhal number} \quad (3)$$

$$\pi_2 = \frac{UD}{\nu} \text{ Reynolds number where } \nu = \frac{\mu}{\rho} \quad (4)$$

Hence:

$$\frac{fD}{U} = F\left(\frac{UD}{\nu}\right) \quad \text{or } St = F(Re) \quad (5)$$

This function must be found by experiments, which is already done and reported by several authors, for instance as shown in Figure 2.

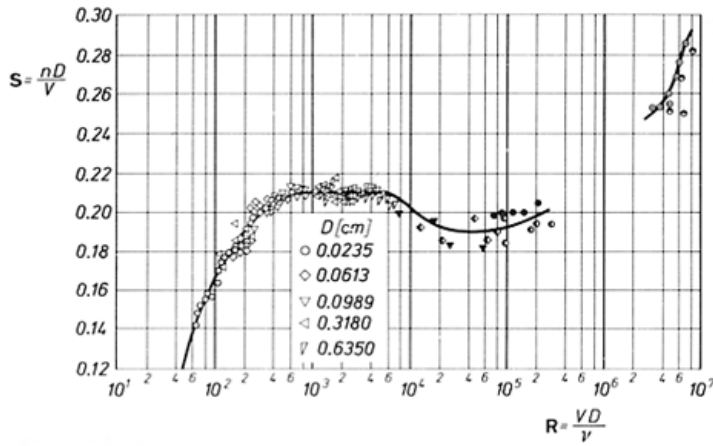


Figure 2 Strouhal number as a function of Reynolds number according to Schlichting (Ref. 4)

The figure indicates a constant $St = 0.21$ for $400 < Re < 6000$ and $St = 0.19$ for $10^4 < Re < 10^5$.
 Then:

$$\frac{fD}{U} = \text{constant} \quad \text{hence:} \quad f = \text{constant} \frac{U}{D} \quad (6)$$

Analytic formulas for calculating frequency have been presented by several authors. The frequency by Strouhal formula, with Strouhal number as a constant equal to 0.2 is one approach that Gongwer (Ref. 1) modified by experiments in order to make it suitable for runner blades:

$$f = St \frac{U}{(t + \delta_v)} \quad (7)$$

δ_v is a virtual boundary layer thickness to be added to the blade thickness, t , which is found by experiments on runner blades with circular trailing edge to be:

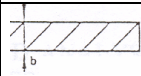
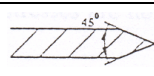
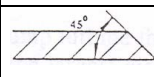
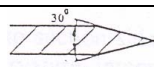
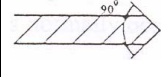
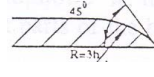
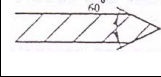
$$\delta_v = 0.0293 \frac{x}{(Re_x)^{1/5}} \quad (8)$$

Gongwer introduced the blade length, x , and the Reynolds number, Re_x , is the Reynolds number based on the blade length. By adding δ_v to the blade thickness, Gongwer found that $St = 0.19$ is more appropriate. Based on the work of Gongwer (Ref. 1) and Donaldson (Ref.

2), Heskestad/Olberts (Ref. 3) did additional experiments and other outlet edge geometries. These experiments concluded in the formula:

$$f = St \frac{B}{100} \frac{U}{(t + \delta_v)} \quad (9)$$

B is a relative frequency. It is dependent on the trailing edge shape as shown in Tabular 1.

Plate	Geometry	B	Plate	Geometry	B
1		100	5		117
2		112	6		159
3		96	7		149
4		93			

Tabular 1 Relative frequency B for different geometries

CFD calculations

A CFD model was set up in order to calculate the frequencies at these different geometries and to find out if CFD calculations would comply with the mentioned formulae.

The simulations were carried out in the commercial program Fluent 6.0. Because of the time-dependent simulations, a laminar model was used. The geometry was as close to the original experimental geometry as possible, as shown in Figure 3:

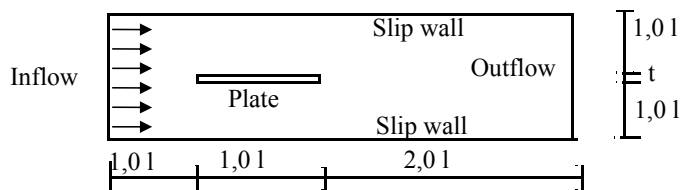


Figure 3 Sketch of the geometry

This model requires approximately 100000 square grid cells and in 2D it takes about 20 hours CPU time to finish one case of simulation, dependent on the computer speed.

The 3D results were as good as identical to the 2D results, but far more time-consuming. A typical 3D-grid requires circa 10^6 grid cells and about 3 weeks of CPU-time per case. Since

the results differed negligible, 2D simulations were of course preferred considering the time aspect.

The calculation results were analyzed by examining the oscillating pressure at 18 different points immediate downstream the trailing edge as shown in Figure 4.

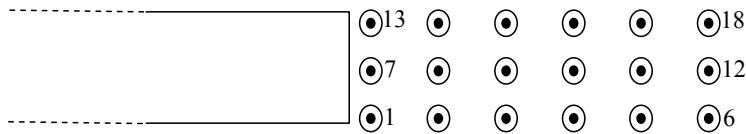


Figure 4 Sketch of pressure points.

A perfect match to the frequency deduced by the formula suggested by Heskestad/Olberts was not achieved. A deviation that was only slightly dependent on the parameters in formula (9) was found. The deviation varied with the trailing edge geometry as shown in Tabular 2.

Plate	Geometry	f _t /f _{sim}	Plate	Geometry	f _t /f _{sim}
1		1.15	5		1.23
2		1.36	6		1.18
3		1.27	7		1.21
4		1.10			

Tabular 2 The ratio between the empirical calculated and the simulated frequency.

What about the amplitude?

The simulated amplitude values seem to have no connections to the frequency, and the influence of the trailing edge geometry to the amplitude is also difficult to determine. However, for each geometry case the calculated amplitudes seem to be reasonable. The amplitude values are a bit dampened close to the plate, with the highest value in the second point after the trailing edge, and then fading out further downstream, as seen in Figure 5.

Studying the results closely, some interesting facts can be seen. The pressure variation in points 1-6 are in anti-phase to the pressure in points 14-18. This makes sense, considering the alternate shedding from the upper and lower side respectively. The amplitudes have also nearly the same value. The points in the middle will be affected by both the vortices and will therefore have a frequency twice as large as the other points, and amplitude close to zero since the upper and lower vortices will counteract each other. This fact is valid for a symmetric trailing edge only. For an asymmetric trailing edge, the vortices do not shed symmetric on the

edge; hence the upper and lower vortex will not be in perfect anti-phase. This may reduce the risk for resonance and fatigue failure.

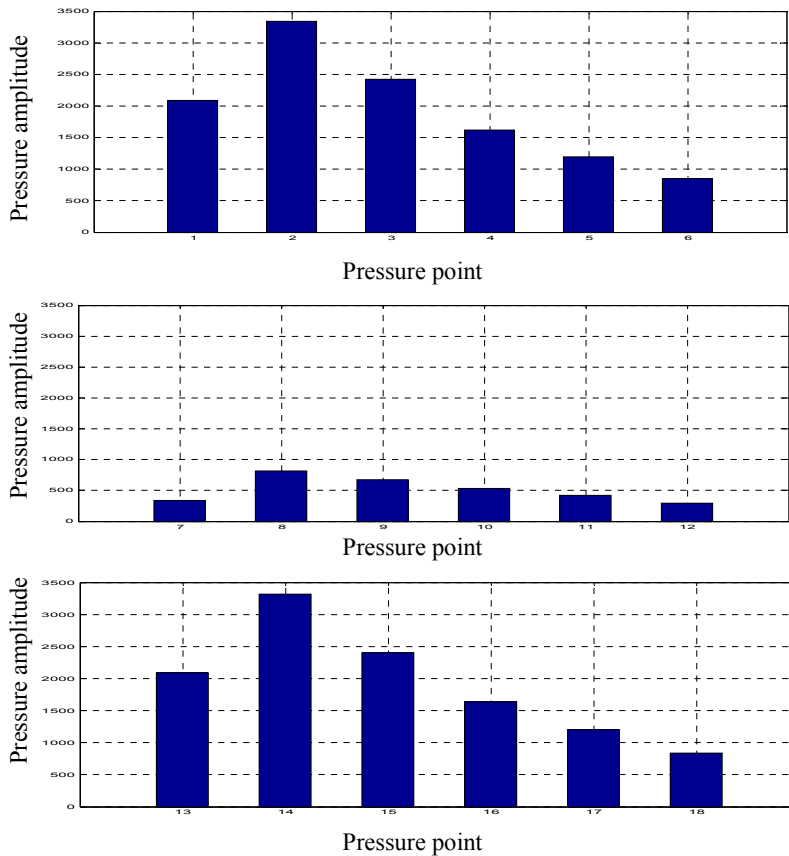


Figure 5 Amplitude plot at position 1-18 with reference to Figure 4.

The common practice when designing the trailing edge is to assume that high frequency gives low amplitudes. This implies an assumption of constant energy in the fluctuation independent on the frequency.

Neither experiments nor the CFD calculations verify this assumption. The frequency is linearly dependent on geometry and velocity. The amplitude has no similar trend.

A very simplified analogy to this is an oscillating pendulum where the amplitude is totally independent of the frequency and visa versa. The amplitude is only given by how fare out of equilibrium the pendulum is moved before it is let go. After a while the amplitude will be dampened out by the friction losses. In other words, it is an external enforce disturbance that sets the pendulum in motion and defines the amplitude. So what is the external enforced disturbance that defines the amplitude of the vortex train? It is reasons to believe that the free

stream velocity, U , plays an important role. Using a dimensional analysis again might give a certain understanding.

For flow around a cylinder with diameter D , it might be assumed that the amplitude, which must be understood as the pressure amplitude, is a function of frequency, diameter, density, dynamic viscosity and velocity:

$$\Delta p = F(f, D, \rho, \mu, U) \quad (10)$$

There are $6 - 3 = 3$ π -groups to be identified. We already have the Reynolds number and the Strouhal number.

The dimension of the pressure amplitude is N/m^2 or $\text{kgm/s}^2\text{m}^2$. Combining it with the other properties in order to form a dimensionless number a suggestion of the 3rd π -number comes forth:

$$\pi_3 = \frac{\Delta p}{\rho U^2} \quad (11)$$

For steady state flow, this number is often referred to as the pressure number. Here, however, Δp is a pressure oscillation, not a steady state pressure.

According to Buckingham's pi-theorem:

$$\pi_3 = F(\pi_1, \pi_2) \quad (12)$$

or:

$$\frac{\Delta p}{\rho U^2} = f(R_e, St) \quad (13)$$

Using the common assumption, which is at least partly verified in experiments, that the Strouhal number is a constant within a certain Reynolds number region. The simplest equation then becomes:

$$\frac{\Delta p}{\rho U^2} = \text{const} \cdot f(R_e) \quad (14)$$

The CFD calculations, however, shows that the pressure amplitude number is also independent of Re number, hence:

$$\frac{\Delta p}{\rho U^2} = \text{const} \quad (15)$$

The results of the CFD calculations are shown in Figure 6 where Δp is defined as the pressure difference between the two sides of the blades. Because of the lack of quality experimental data in this case, it is hard to say how good the CFD results really are. Experiments that will verify whether this is correct or not are planned to be carried out in the close future.

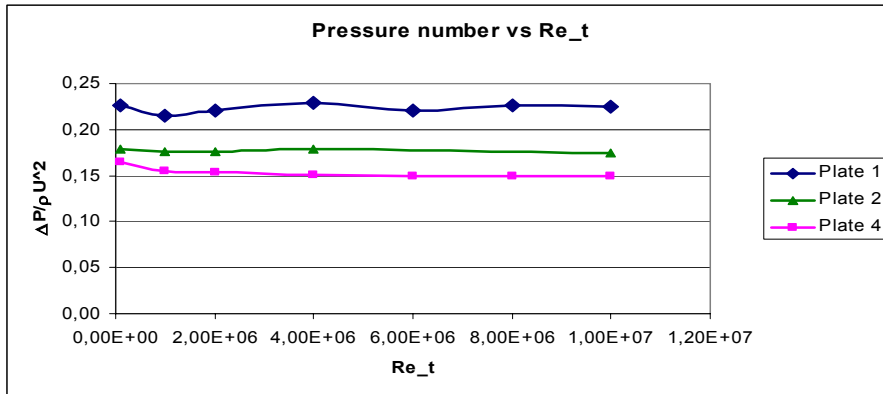


Figure 6 Pressure number as a function of Re number

Conclusion

CFD calculations of the frequency of von Karman vortex streets are very much in accordance with the formula suggested by Heskestad/Olberts (Ref. 3). A correction factor is however suggested.

It seems that for a given trailing edge geometry, the pressure-amplitude number is more or less constant with respect to both Strouhal and Reynolds number.

Our suggestion is therefore that the pressure amplitude can be determined by the formula:

$$\Delta p = \beta \rho U^2 \quad (16)$$

where β is a constant which will vary with the local geometry of the trailing edge. This must of course be confirmed by experiments.

References

- 1) C.A.Gongwer : A Study of Vanes Singing in the Water, Transaction of ASME, Volume 74 1952.
- 2) R.M.Donaldson: Hydraulic-Turbine Runner Vibration, Transactions of the ASME Jan. 1957
- 3) G.Heskestad, D.R.Olberts: Influence of Trailing-Edge Geometry on Hydraulic Turbine Blade Vibration Resulting From Vortex Excitation, Transactions of the ASME, April 1960
- 4) H.Schlichting: Boundary-Layer Theory, McGraw-Hill, Inc1987

A.2 Hydrovision Portland, Oregon, USA, 2006

Experimental and theoretical investigations of the flow field at the inlet of a Francis runner

**By Øyvind Antonsen, Torbjørn K Nielsen and Ole G Dahlhaug.
Norwegian University of Science and Technology**

Abstract

This paper presents and discusses CFD simulations performed in order to investigate the dynamic load inflicted to the runner blade by the outflow from stay vane and wicket gate. The CFD simulations are compared to the results from laboratory experiments in a blade cascade. LDV-measurements of velocity distribution in a cascade for various guide vane profiles were carried out. Later, pressure pulsations in a model turbine where the different guide vane profiles were implemented, was investigated. This is not treated in this paper.

For the experiments, a special test rig with is a 1:2.5 scaled homologous model of the last quarter of a high head Francis turbine, including 5 stay vanes and 5 guide vanes, was used. The velocity profile between the guide vanes were measured by LDV.

An overall goal of this project is to improve the accuracy of the theoretical predictions of the dynamic pressure fluctuations at the boundary between the distributor and the runner. A better prediction of the oscillating forces on the blade is essential in order to secure structural safety.

Preface

The trend towards higher speed and higher output has increased the potential for fluid/structure interaction problems, and the severity of those problems. Under certain conditions these interaction phenomena can lead to structural failure. Turbine manufactures have in recent years experienced several serious runner blade cracking due to high dynamic stress level at runner inlet. The main source of instability at the boundary between distributor and runner is the wake flow from the guide vanes that is chopped by the runner blades, causing oscillating forces. Therefore, an improved prediction of these dynamic forces would be of great value in order to avoid fatigue problems on the runner in the future.

In order to investigate this phenomenon a series of laboratory experiments and CFD-calculations has been performed. The experiments were carried out at the Waterpower Laboratory at the Norwegian University of Science and Technology (NTNU).

Hypothesis

The dynamic force acting on the runner blade is assumed to be dominated by two different phenomena, the viscous effect, and the pressure effect. The viscous effect is due to the velocity defect in the flow because of the shadow from the up stream guide vane. The disturbance of the velocity will be smaller as the distance increases; hence a certain minimum distance between the guide vanes and the runner is recommendable.

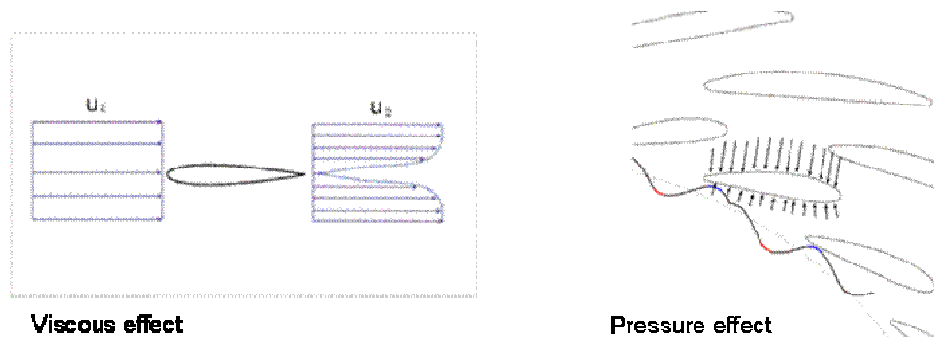


Figure 1 Velocity variation in the shadow of the guide vane

The pressure effect can be explained by the fact that the high pressure on the up-stream side will give local high pressure zones in the cave between the wicket gate and the runner.

By profiling the guide vanes so that the pressure side and suction side counteracting the global pressure, the overall pressure variation at the inlet of the runner will be reduced resulting in less pulsating load on inlet of the runner blade.

However, optimization with respect of the dampening the pressure fluctuation, will not necessarily give the optimal efficiency. The final design will be a compromise between these objectives.

CFD simulations verified by measurements

In order to verify the CFD simulations by means of LDV measurements, a 1:2.5 model of a high head Francis turbine used in a previous experiment was used. The model is of acrylic plastic and is a homologous model of the last quarter of the stay vane and guide vane cascade, including 5 stay vanes and 5 guide vanes. The model is shown in Figure 2

The velocity profile between the guide vanes was measured for different guide vane profiles and compared with the CFD simulations.

The main goal of the calculations was to calibrate verify the CFD simulations of the same geometrical model with velocity measurements and then do further calculations with CFD both of pressure and velocity of various guide vane profiles.

The CFD calculations were carried out with the commercial program Fluent 6.2. A simplified model consisting three stay- and three guide vanes was used in the calculations. First it was run a set of simulations close to the measurements in order to “calibrate” the CFD-model, and afterwards, a set of simulations to calculate the pressure distribution as a function of the guide vane-profiling where carried out. The results are presented in the following chapters.

Measurements

The experiments consisted of a series of LDV-measurements (Laser Doppler Velocimetry) of the wake of at guide vane in a double cascade. The wake was measured downstream guide vane no 3, at different downstream lengths and varying flow. Two different guide vane profiles where used, one symmetric and one asymmetric. The flow was regulated both by adjusting the feeding pump and the throttling valve at the outlet of the cascade. A two component AR-ion Laser was used to gather data and post processing was done with programs such as Matlab and LabView. During the measurements, the LDV-probe was traversed in small steps in horizontal direction, measuring the velocity in each step. For each step, a number of 5000 valid points was sampled and the velocity was then calculated as the average of this points. The probe was traversed in several distances downstream the guide vanes and with different flow, guide vanes-angle and two different profiled guide vanes.

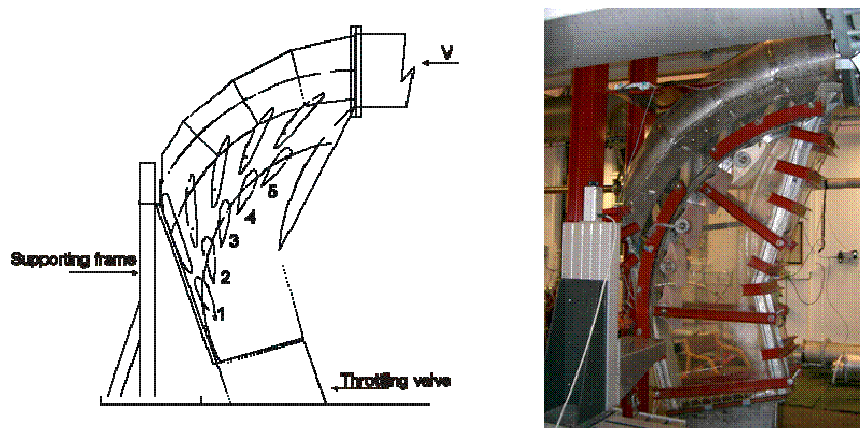


Figure 2 The cascade test rig

CFD results

The CFD calculations confirm that velocity and pressure fluctuations will occur in the cave between the guide vane and the runner. It is assumable that this phenomenon will lead to dynamic loading on the runner blade.

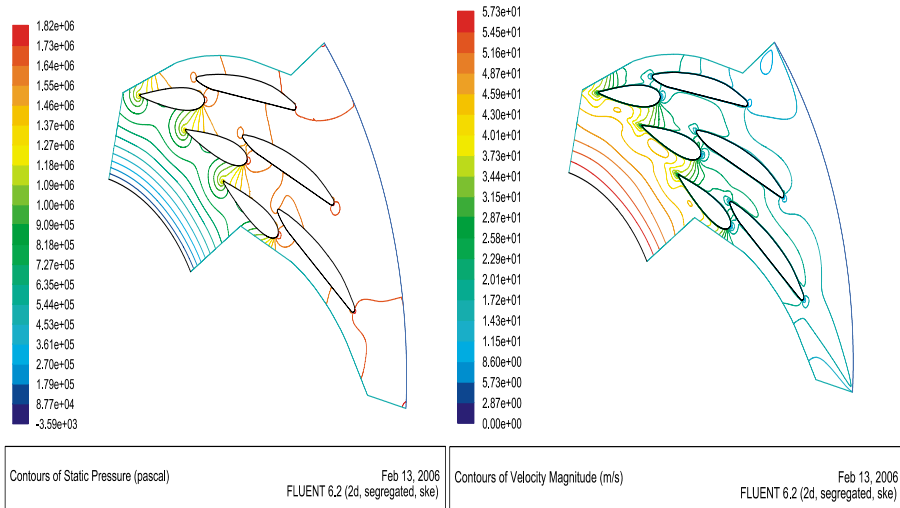


Figure 3 Pressure and velocity distribution in the cascade

Since even an in-viscous calculation gives pressure fluctuations, the presence of the pressure effect should be confirmed. Without the viscosity the flow will have less damping and hence the pressure fluctuations will be higher than with the viscosity present.

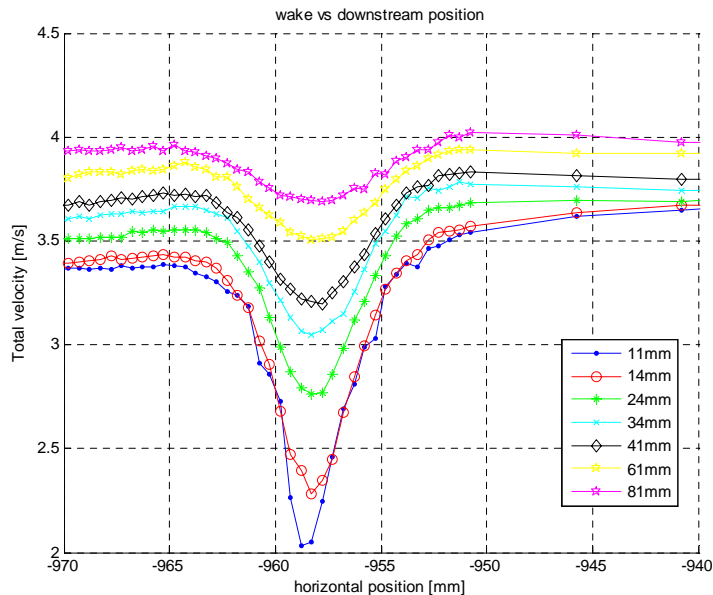


Figure 4 Wake at different downstream positions

Measurement results

An example of the velocity measurements are showed in Figure 4. As expected, the wake will gradually attenuate as the distance from the guide

vane increases. To get a more detailed and general analysis, the form-function is introduced so the velocity can be written as a general function, dependent of the horizontal position only:

$$u_{norm} = a + b \cdot e^{c(x-d)^2} \quad (1)$$

Where u_{norm} is normalized with the free stream velocity in the following way:

$$u_{norm} = -\left(\frac{u - U_0}{U_0}\right) \quad (2)$$

The other parameters are defined in Figure 5.

To get a general expression for the wake, a general function of the coefficients must be found. A plot of the most important coefficient, the velocity defect, b , as a function of downstream length, flow and guide vane-profiling are shown in Figure 6

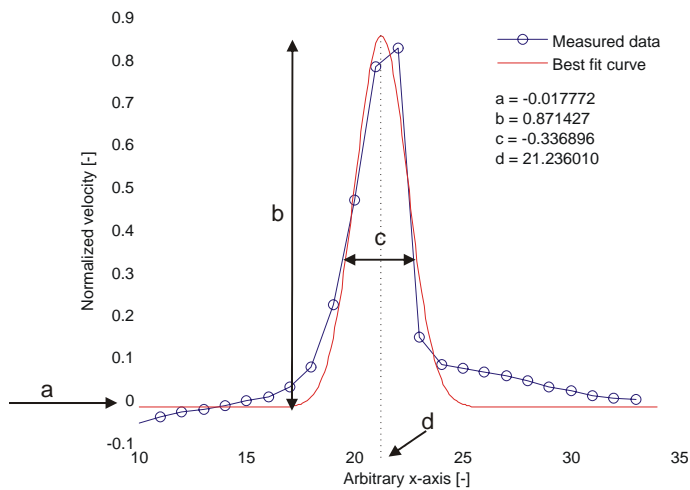


Figure 5 Best fit curve with coefficients

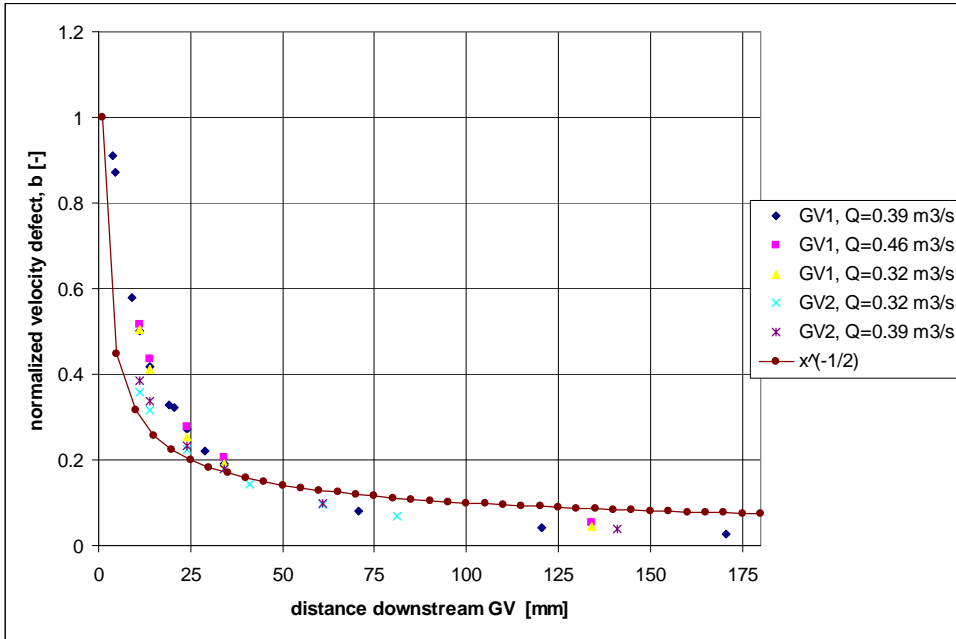


Figure 6 Normalized velocity defect

Two interesting elements can be seen from the results. First, the velocity defect follows the general wake-theory quite well. White [1] , states that the velocity defect in a plane wake follows the expression

$$\Delta U = const \cdot x^{-1/2} \quad (3)$$

A plot of $x^{-1/2}$ is added to Figure 6, and it can be seen that the data follows this curve quite well.

Second, the data have a significant break around 50 mm. It is assumed that the wake-flow consist of two zones. The first stage is a momentum mixing zone where the flow is dominated of the mixing of the pressure difference and the viscous defect. Further downstream the flow is stabilized as pure wake-flow. This is also in agreement with well known wake-theory.

During start up and shut down of the rig, the pressure in the rig was lowered so air bubbles were visible in the water. At this operation point, a vortex was observed at the inner curve, approximately at the height of guide vane no 3 and no 4. Unfortunately this point was outside the range of the traversing of the LDV-equipment, so it could not be confirmed whether this vortex was present during the measurements.

The LDV can only measure velocity, to get information of the pressure-variation, CFD is used. To validate the CFD-calculations, they are compared with the LDV-data.

Comparison lab and CFD

A direct comparison of a velocity-plot from lab and CFD respectively are shown in Figure 7

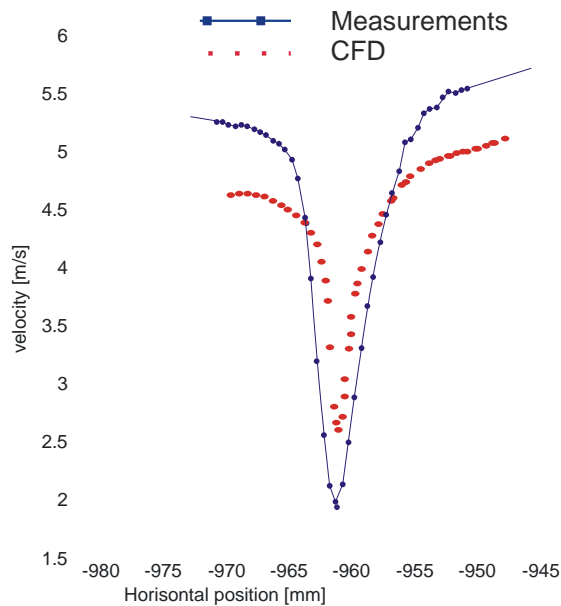


Figure 7 Comparison CFD and LDV-measurements

It is clear that the CFD under predicts the velocity in the flow. That may be caused by the vortex in the cascade as mentioned above. The CFD shows no vortex, and since the presence of this will increase the velocity because of a smaller effective area, the velocities will be higher. The inlet boundary condition for the CFD is the flow, and with the same flow but without the vortex, the velocities will be smaller.

However; when the CFD-results are normalized in the same way as the measurements, they follow the wake-theory quite well. 0 shows a comparison between the normalized values from CFD and lab-results respectively.

Even though the lab and CFD results don't show exactly agreement, they show the tendency in the flow in the same way. That means that the CFD results are trustworthy, but should be used by care, especially when it comes to absolute quantities.

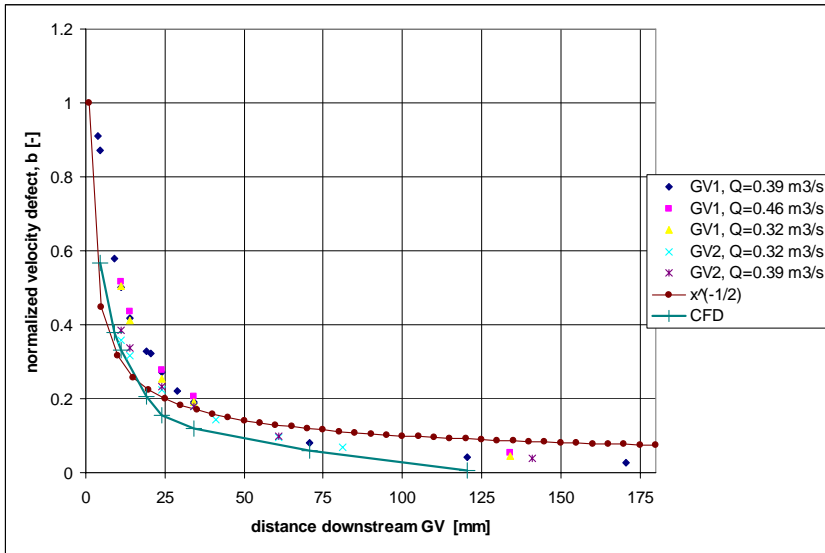


Figure 8 Normalized velocity defect from measurements and CFD

CFD of different guide vane profiles

Since the CFD simulations now can be considered reliable after the verification by LDV measurements, the hypothesis of guide vane-profiling versus pressure pulses can be simulated. Three different guide vane profiles, as showed in Figure 9.

The pressure variation at the outlet of the guide vanes, presented as normalized pressure in percentage of the total head, is shown in Figure 10. It can clearly be seen that the profiling of the guide vane has influence on the overall pressure distribution. The results also show good agreement with the hypothesis on the fact that a local pressure and suction side will counteract the global pressure field and hence reduce the load on the runner.

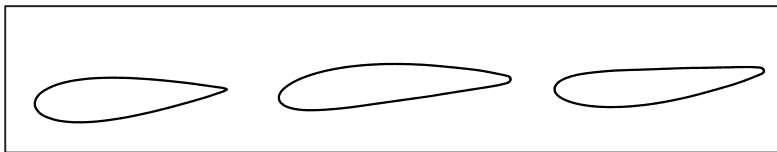


Figure 9 Guide vane profiles. Symmetric, Asymmetric1 and Asymmetric 2

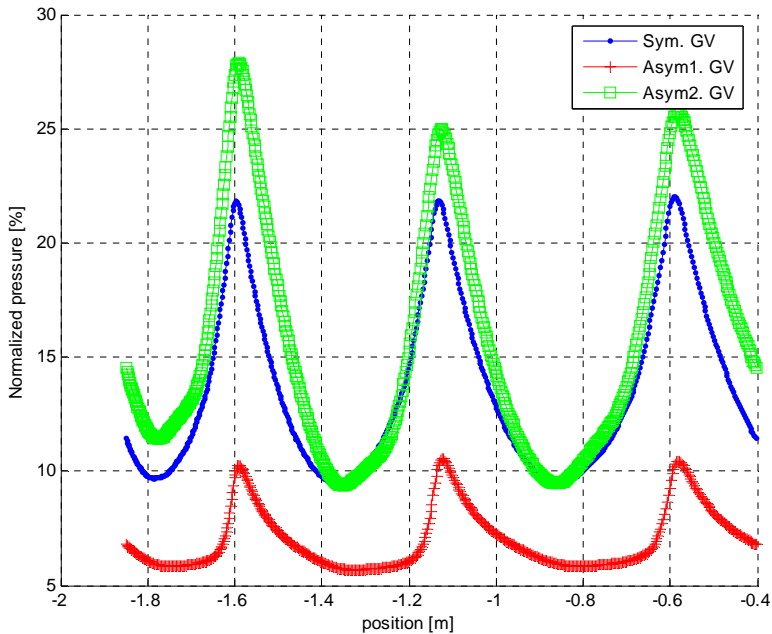


Figure 10 Pressure distribution with different guide vanes

Discussion

It is confirmed that the load on the runner inlet, due to pressure pulses is dependent of the guide vane-profiling. The hypothesis, that the total load consists of a viscous part and a pressure part, seems also to be verified.

More uncertain is the importance of the two parts and in what way they load the runner. The viscous part may affect the runner more by varying the relative velocity then the velocity-defect it selves.

The guide vane-angle will than be of importance, both by setting up the relative flow and for the distance between the guide vane and the runner inlet.

Conclusions and further work

Since the main purpose of the guide vanes is to set up the correct flow for the runner, it seems that the profiling of the guide vanes must be a compromise between reducing the pressure pulses and tuning the efficiency to a maximum. The simplest solution, increasing the distance between the guide vanes and the runner, implies that the size of the whole spiral casing must increase. This is very costly and not a relevant solution. By profiling the guide vanes with a local pressure- and suction side counteracting the global pressure and suction side, the overall pressure pulses will decrease. However this may affect the efficiency in a negative way.

To further investigate the relations between guide vanes-profiling, pressure pulses and efficiency there is ongoing work right now. Pressure pulses and efficiency are measured in a model turbine with the same guide vanes - profiles as used in the LDV-measurements.

References

[1] White, Frank. Viscous fluid flow. McGraw-Hill. 1991

Aknowlegdement

The authors wish to thank Morten Kjeldsen for his support during the work of this paper.

Authors

Øyvind Antonsen is PhD-student at the water power lab at the Norwegian University of Science and Technology (NUST). His work includes general pressure pulses in Francis turbines and unsteady load at the inlet of the runner in particular.

Torbjørn K. Nielsen is a professor at Norwegian University of Science and Technology, NTNU, since 2002. His main topic is hydraulic machinery, including the responsibility for The Waterpower Laboratory.

Ole Gunnar Dahlhaug is an associate professor at the Waterpower Laboratory at Norwegian University of Science and Technology, NTNU, since 1999. His main topic is design, maintenance and development of hydraulic machinery.

A.3 IAHR Yokohama Japan, 2006

Pressure Pulses in Francis Turbines vs. Guide Vane Design

Øyvind ANTONSEN* Norwegian University of Science and Technology (NTNU)
oyvind.antonsen@ntnu.no
Torbjørn K. NIELSEN NTNU
torbjorn.nielsen@ntnu.no
Ole G. DAHLHAUG NTNU
ole.g.dahlhaug@ntnu.no
Jan T. BILLDAL GE Energy
jan.billdal@ps.ge.com

Key words: Pressure pulses, Francis turbine, Guide vane design.

Abstract

In order to investigate the pressure pulses at the inlet of a Francis runner, unsteady pressure measurements are carried out in the volute region between the outlet of the guide vanes and the inlet of the runner in a model turbine. The results show that the dominant pulse in this area is the blade passing frequency. By removing the splitter blades on the runner or adding end sealing on the guide vanes, the pressure pulses was changed and gave higher pressure pulses, while smaller changes on the guide vanes or stay vanes did not affect the results.

Introduction

Vibrations at the inlet of a Francis turbine runner caused by the interaction between the runner and the guide vanes are a well known phenomenon. However it is still experienced problems with high sound level and runner blade cracking due to this kind of vibrations. The trend with more kW power per kg turbine also makes the turbines more vulnerable for damage due to vibrations.

The flow in the volute region between the outlet of the guide vanes and the inlet of the runner has a complex flow field, consists of vortex gates from the guide vanes, horseshoe vortices at the upper and lower cover due to the boundary layer and pressure variations over the guide vanes, leakage flow between the guide vanes and upper and lower cover, pressure difference over the guide vanes, both due to the accelerated flow and the profiling of the guide vanes and finally the influence of a rotating runner. All these factors will influence on the total pressure load on the runner, but in different extent depending on the design of the turbine.

In order to dig deeper into this field, a PhD-study has carried out at the Water Power Lab at the Norwegian University of Science and Technology. The study consists of a part with LDA-measurements of the wake of different guide vane profiles and a part with unsteady pressure measurements in the volute region between the outlet of the guide vanes and the inlet of the runner. The results from the LDA measurements are presented in a paper to the Hydrovision 2006, Portland (Ref 1). This paper will focus on the results from the unsteady pressure measurements.

Theory

In the volute region between the outlet of the guide vanes and inlet of the runner, the influence on the flow field is mainly governed by the guide vane wakes and the rotating runner blades. The runner blades will rotate through a non uniform velocity- and pressure field, due to the wake of the guide vanes, causing pressure pulses on the runner blades. Chen (Ref 2) measured the velocity profile at the inlet of the runner and concluded that the velocity profile is neither uniform in circumferential nor in the span wise direction. Hence, the presence of guide vanes in the flow will disturb the flow and set up a non uniform flow field in which the runner blades rotate. This will cause a varying load on the runner blades, dependent of the flow, profile of the guide vanes, the distance between the guide vanes and the runner and the rotational speed of the runner.

At the outlet of the guide vanes, the pressure field is non-uniform both due to the acceleration of the flow and due to the local pressure and suction side of the guide vanes. It is assumed that by profiling the guide vanes with pressure and suction sides that counteracts the global pressure variation, the overall load on the runner blades will be reduced. LDA measurements and CFD-calculations by Antonsen et al. (Ref 1) confirm that the pressure variations will be smaller with the right profiling of the guide vanes.

Experiments by Jernsletten, (Ref 3), also confirm the guide vanes influence on the runner blades. By measure the load on the runner blades before and after cutting the inlet of the runner, the load on the runner was reduced with $\frac{1}{3}$ by increasing the radial distance with 5.1 mm.

The runner blades will also create a change in the flow field due to its rotation. A stationary point will sense a change in pressure each time a runner blade passes the point. This change of pressure causes pressure waves which are propagating around the circumference.

When designing turbines, it is important to choose the number of guide vanes and runner vanes carefully to avoid amplifying and resonance of this pressure wave. It is desirable that as few runner blades hits a wake at the same time. It is also important that the wave don't propagate to the next wake at the same time as a runner blade hits the wake and so build up a larger wave. Lund, (Ref 4), described the pressure wave's propagation by a range of Fourier series. Hence, combinations of favorable and unfavorable numbers of guide vanes and runner blades could be calculated.

Experiment

The measurements were carried out on a model of a high head Francis turbine with 23 stay vanes, 23 guide vanes, and a runner with 15 blades, and 15 splitter blades.

Three piezoelectric pressure transducers were mounted flush with the lower cover between the outlet of the guide vanes, and the inlet of the runner, see Figure 1. These transducers only measure changes in pressure, but is excellent for finding frequency and amplitude in such measurements due to their small size and fast response. For some test series one of the transducers was placed in the draft tube cone in order to

investigate the pressure pulses here. However, the analysis of these results is not completely finished and is omitted from this paper. A range of different operating points were measured. Also several mechanical modifications on the turbine were carried out. A short outline of the most interesting results is given in the following sections.

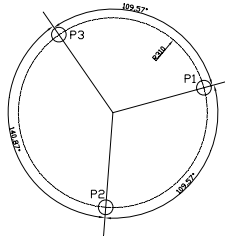


Figure 1 Placing of pressure transducers

By placing the pressure transducers in the lower cover as shown in Figure 1, it is reasonable to assume that the dominant frequency will be the blade passing frequency, given by equation (1), and harmonics of this.

$$f_b = \frac{z_r n_r}{60} \quad (1)$$

Where

- f_b [Hz] is the blade passing frequency
- z_r is the number of runner blades
- n_r [rpm] is the rotational speed of the runner.

A pressure wave will propagate in the water with the speed of sound, and can be traced in the measurements with an expected frequency of

$$f_1 = \frac{v_1}{O} = \frac{a+u}{O} \quad \text{and} \quad f_2 = \frac{a-u}{O} \quad (2)$$

Where

- f [Hz] is the expected frequency
- a [m/s] is the speed of sound in water
- u [m/s] is the velocity of the water in circumferential direction.
- O [m] is the circumference of the volute region.

The pressure transducers are placed at the same relative distance from a guide vane but non-symmetric around the circumference. The reason for this is to capture any superimposed pressure waves as described in equation (2).

Results

The signals were sampled with a sampling frequency of 6000 Hz and sampling time of 10 seconds to ensure that both high- and low frequencies could be traced. A power spectrum analysis was carried out on the signals in order to find the dominant frequencies and their strength. Fast Fourier Transform (FFT) using the Welch method

with a window size of 2^{13} and overlap of 66% ensured that no information was lost. Figure 2 shows a typical pressure-time plot with corresponding FFT-plot. The frequency axis is normalized with the expected blade passing frequency, given by equation (1).

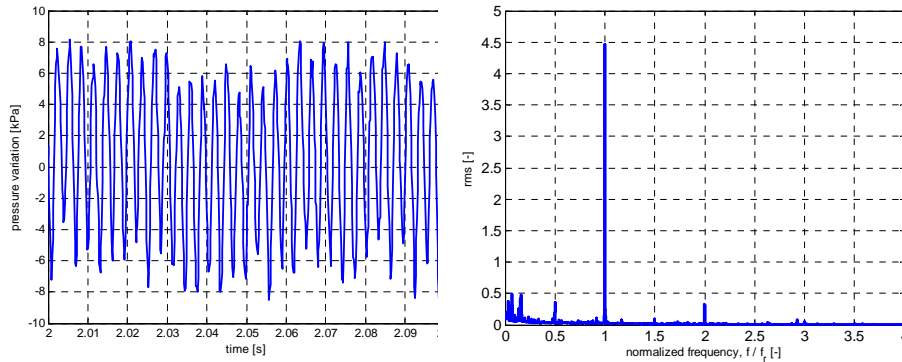


Figure 2 Results from the measurements

It is clear that the blade passing frequency is the dominant frequency in the measured area. Both higher harmonics and a sub-harmonic are also present, together with 50 Hz noise from the electric grid and some low frequency noise. Measurements from the three different transducers show almost identical results, only shifted in time by the expected time lag, given by equation (3). For all the measurements, ca 400 measurement series, the maximum deviation from the theoretical blade passing frequency was 0.40 Hz. There was no trace of frequencies from equation (2), which means that the blade passing frequency is the dominant frequency and that the pressure waves are died out before they travel one revolution.

$$\Delta t = \frac{\Delta \phi \cdot 60}{360 \cdot n} \quad (3)$$

Where

Δt [s] is the time lag

$\Delta \phi$ [deg] is the angular distance between a runner blade and a transducer

n [rpm] is the rotational speed of the runner.

Neither changes in the stay vane angles nor modifications of the runner cone had no impact on the pressure pulses at the inlet of the runner. The radial distance between the guide vanes and runner was the same for all measurements. The level of the pressure pulses are generally low, which means that this turbine is well designed and has no problems with pressure pulses at the inlet of the runner. The two sets of guide vanes tested were too similar in design to give any changes in the results. Two modifications gave significant changes in the pressure pulses; that is the elimination of the splitter blades and the use of end sealing on the guide vanes. A plot of these results is shown in Figure 3. The pressure pulses are presented as peak to peak values in meters water column normalized with the total head. Results from three different

unit speeds, n_{11} , are shown. The unit speed is defined in equation (4). The turbine has best efficiency point at $n_{11} = 36$.

$$n_{11} = \frac{n \cdot D}{\sqrt{H}} \quad (4)$$

Where

- n [rpm] is the rotational speed of the runner
- D [m] is the outlet diameter of the runner
- H [m] is the head of the turbine

For the original geometry, the highest pressure pulses are found at full load at $n_{11}=32$. It seems that the pulses are lower the higher the n_{11} level is. At $n_{11}=36$, the curve is rather flat over the whole operation range, which indicates that the turbine is well designed and that the splitter blades contributes to an even pressure variation. It can also be seen that the level of the pulses are lower the higher the unit speed is.

The results from the runner without the splitter blades show a quite different behavior. The pulses seem less dependent of n_{11} and even though the curves differ, it is no clear trend among them. Compared to the original runner, the pulses are lower at very low load while they are higher at part load and full load. At $n_{11}=36$, the pulses without splitter blades reaches a higher level than the original runner at about $0.80Q^*$. (Q^* is the best efficiency point).

With end sealing on the guide vanes, the curves for $n_{11}=36$ and 40 are rather flat but on a higher level than without end sealing, while the curve for $n_{11}=32$ are quite scattered.

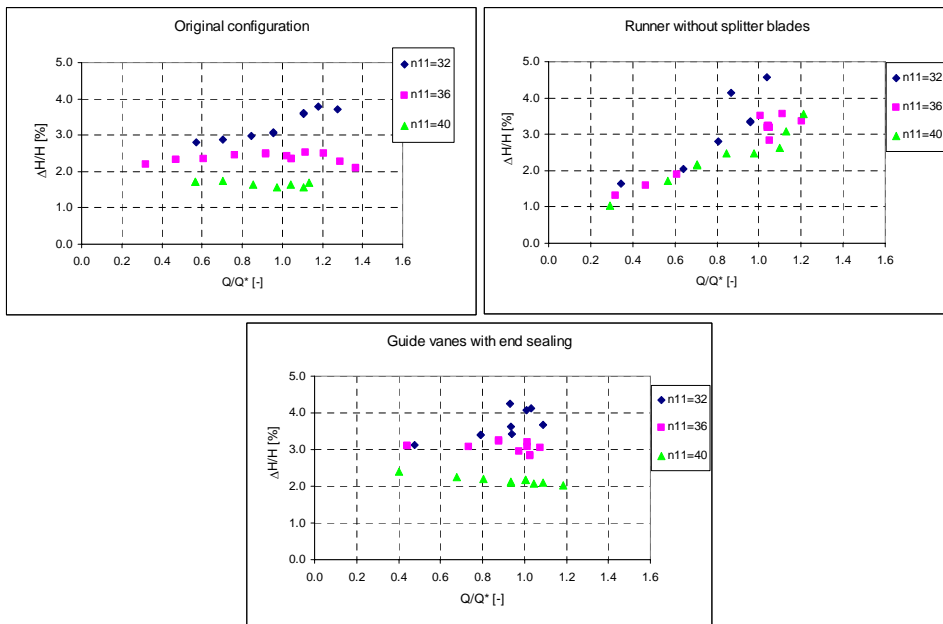


Figure 3 Results

One noteworthy fact is the increase of pressure pulses with the added end sealing on the guide vanes. The end sealing will reduce the clearance flow between the guide vanes and the upper and lower cover. This will give less disturbance of the main flow field and hence higher efficiency of the turbine. However, this clearance flow might contribute to a faster mixing of the guide vane wake and hence reduce the pressure pulses on the runner.

By removing the splitter blades on the runner, the best efficiency point of the turbine was shifted towards higher n_{11} . Hence the curve for $n_{11}=40$ in Figure 3 is closer to the best efficiency point than the $n_{11}=36$ curve. Without the splitter blades the pressure variation between suction side and pressure side of the runner blades are bigger than with splitter blades. With a bigger pressure difference rotating with the runner, it is reasonable that the pressure pulses are higher for this case.

Since this turbine generally has low pressure pulses and since it needed quite large modifications before any change in the pressure pulses occurred it might not be the best model to find trends in the pressure pulses. However it is no doubt that at the inlet of the runner it is the blade passing frequency that is the dominant factor.

Conclusions

Unsteady pressure measurements in a model of a high head Francis turbine have been carried out. The results show that at the inlet of a Francis runner, the pressure pulses are dominated by the blade passing frequency. For this turbine the level of pressure pulses was rather low over the whole operation area. This is according to the expected results since the guide vanes are slightly asymmetric profiled with a pressure side counteracting the pressure field set up by the accelerating flow. This gives a quite uniform pressure field for the runner blades to rotate in and hence a low level on the pressure pulses.

By adding end sealing on the guide vanes, it will be less mixing of the guide vane wake and this will contribute to a higher level of pressure pulses. By removing the splitter blades, the pressure difference between the suction side and the pressure side of the runner will increase and hence the pressure pulses will increase.

Unfortunately the difference in the two sets of guide vanes was not big enough to give any changes in the pressure pulses. In order to further confirm the hypothesis and to investigate the flow field at the inlet of the runner, CFD-calculations and further analysis of the measurement data will be carried out.

References

- (Ref 1) Antonsen, Nielsen and Dahlhaug. *Experimental and theoretical investigations of the flow field at the inlet of a Francis runner*. Hydrovision 2006, Portland Oregon.
- (Ref 2) Xin Chen. *Theoretical and experimental study of flow through the double cascade of a Francis turbine*. PhD-thesis. Norwegian Institute of Technology. 1992.
- (Ref 3) Jernsletten, Jo. *Analysis of non-stationary flow in a Francis reversible pump turbine runner*. PhD-thesis. Norwegian Institute of Technology. 1995.
- (Ref 4) Lund, Emil. *Hydrauliske trykksvingninger i omdreiningshulrommet mellom løpehjul og ledeapparat i en Francis turbin*. (in Norwegian). Lisentiatarbeid, Norwegian Institute of Technology. 1966